Spectral Ageing in Powerful Radio Galaxies

Sivakumar G. Manickam

National Centre for Radio Astrophysics (TIFR),

Post Bag 3, Ganeshkhind, Pune 411 007.

Thesis Guide: Dr. D.J. Saikia

Thesis submitted in partial fulfillment of

Master of Science in Physics (PPPR),

University of Pune.

March 1998.

Declaration

I declare that the work presented in this thesis, entitled "spectral ageing in powerful radio galaxies", has been carried out by me at the National Centre for Radio Astrophysics, Tata Institute of Fundamental Research, Pune. This work has been been carried out in partial fulfilment of the requirements for the completion of the course for Master of Science in Physics (Partly by Papers and Partly by Research) of the university of Pune. No part of this work has been submitted for the award of any other degree or diploma.

M. G. Sivakumar

Sivakumar G. Manickam

Certificate

This is to certify that the work presented in this thesis, entitled "Spectral ageing in powerful radio galaxies", has been carried out by Shri Sivakumar G. Manickam at the National Centre for Radio Astrophysics, Tata Institute of Fundamental Research, Pune. This work has been carried out in partial fulfilment of the requirements for the completion of the course for Master of Science in Physics (Partly by Papers and Partly by Research) of the University of Pune. No part of this work has been submitted for the award of any other degree or diploma.

D.J. Saikia

Thesis Guide

Through

V.K. Kapahi

Director, NCRA

Acknowledgements

I thank Dr. D.J. Saikia for his guidance while working on this thesis. I am grateful to Dr. Jayaram Chengalur, Prof Gopal-Krishna, Prof. Vasant Kulkarni and Prof. A. Pramesh Rao for reading the drafts of this thesis and for their comments and suggestions. Many thanks to Ishwar and Ramana for their help in getting conversant with *AIPS*. I have benefited from several detailed discussions with Prof. Gopal-Krishna.

Contents

Acknowledgements iii

Synopsis vi

1. Introduction 1

1.1 Radio structures of radio galaxies and quasars 4

1.2 Outflow pattern 7

1.3 Spectral ageing and ages of radio sources 8

1.4 Outline of this thesis 9

2. Spectral Index Evolution 11

2.1 Energy loss mechanisms for high energy electrons 12

2.1.1 Ionisation losses 12

2.1.2 Bremsstrahlung 12

2.1.3 Adiabatic losses 13

2.1.4 Synchrotron radiation 13

2.1.5 Inverse Compton scattering 14

2.2 The diffusion-loss equation for high energy electrons 14

2.2.1 Instantaneous injection 15

2.2.2 Continuous injection 16

2.2.3 Recurring injection 17

2.3 Indicators of Age 18

2.4 Models for the evolution of the electrons 20

2.5 Difficulties in real sources 21

3. Observations and analysis 23
3.1 Sample of sources 23
3.2 Observations 24
3.3 Calibration of the data 24
3.4 Imaging 25

4. Spectral ageing and concluding remarks 27
4.1 Observational results 27
4.2 Spectral ages of our sources 40
4.3 Earlier estimates of spectral ages from radio images 42
4.4 Other velocity estimates of hotspots 47
4.5 Evidence of ageing at higher frequencies 48
4.6 Concluding remarks 50

References 51

Synopsis

The radio structures of radio galaxies and quasars can be broadly described as consisting of two lobes of radio emission located more or less symmetrically on either side of the parent optical object, and a compact core or nuclear component nearly always coincident with the optical object. In addition, one often finds narrow collimated features called 'jets' connecting the core to the extended components, which are believed to be signatures of the beams carrying energy from the nucleus to the outer lobes. The overall linear sizes of radio sources range from less than a few tens of parsecs to over a Mpc. The radio emission from the lobes as well as the nuclear component is believed to be due to synchrotron emission. The emission from the extended components has a steep radio spectrum ($\alpha > 0.5$, where the flux density $S \propto \nu^{-\alpha}$) and is optically thin, while the emission from the cores has a flat or complex spectrum and is optically thick to its own emission.

The radio galaxies and quasars can be classified into two categories on the basis of their extended radio emission, namely the Fanaroff-Riley or FRI and FRII sources. The FRI sources are of lower luminosity, have diffuse extended plumes of emission, reasonably symmetric large-scale jets and are often brightest closer to the centre. The FRII sources are of higher luminosity ($P_{178} \geq 0.5 \times 10^{25}$ W Hz^{-1} sr^{-1} for H_0=100 km s^{-1} Mpc^{-1}) and q_0=0), have prominent hot-spots at the outer edges which are identified with the regions where the energy-carrying beams interact with the external medium, and the bulk of the energy is deposited.

In the standard twin-beam model for radio sources, the extended lobes of radio emission arise due to backflow from the hot-spots as the beams advance outwards through the interstellar and then the intergalactic medium. Hence the radiating plasma closer to the nucleus would be older than that near the hot-spot and one might find evidence of spectral

ageing across the radio source. This ageing is due to the radiative losses of the electrons responsible for the observed synchrotron emission. The highest energy electrons lose energy more rapidly and unless there is a replenishment of these high-energy particles the spectrum will tend to curve downwards. Thus in the lobes of double radio sources, the spectra would steepen as one goes away from the hotspots along the axes of the lobes. This can be used to estimate the ages of the lobes and the velocity of advance of the hot-spots if the distance to the source is known.

In this thesis we present the observations of 5 FRII radio galaxies selected from the Molonglo Reference Catalogue (MRC) which are generally weaker than the 3CR sources, and examine any evidence of spectral index gradients in order to estimate their ages and velocity of advance of the hot-spots. These observations were made with the Very Large Array (VLA) at the L-band (1365 MHz) with the hybrid CnB array and at the C-band (4635 MHz) with the BnA array. The angular resolutions at the two frequencies are identical, providing reliable information on spectral-index gradients.

The estimates of age and velocity of our sample of 5 sources from the MRC are consistent with the expectations of the standard twin-beam model for radio sources, and values available in the literature for sources of similar luminosity. The source ages are around 8-28 Myr and velocity of the lobes are around 0.5-5 in units of 0.01c (c= 3×10^{8} m/s), including both synchrotron and inverse-Compton losses due to the microwave background radiation. Using our results as well as those from the literature there is a weak trend for the lower luminosity sources to be older, which could be understood in terms of a lower equipartition magnetic field in these sources.

Chapter 1

Introduction

Galaxies are the fundamental building blocks of our Universe. Surveys of the sky at optical and infrared wavelengths show that the nearby galaxies are distributed in an inhomogeneous way, posing interesting questions on the clustering of galaxies and the scale sizes over which the mean distribution of galaxies in the Universe can be considered to be homogeneous, as postulated in the cosmological principle. There have been many theoretical and numerical studies to understand the formation and distribution of galaxies, especially since the results of several large surveys of galaxies became available (cf. Padmanabhan 1993; Sahni & Coles 1995).

Galaxies have a wide variety of shapes and structures. Since the early days when photographic images of galaxies were available, there have been a number of attempts to classify these into different categories. The most widely used classification scheme is the one suggested by Hubble where the smooth and largely structureless galaxies with an elliptical appearance are classified as ellipticals. After the elliptical galaxies, Hubble's classification bifurcates into the normal spiral galaxies and the barred spirals, the latter having a prominent bar in the central region of the galaxy. At the junction of the spirals and the ellipticals are the lenticulars which have a prominent spheroidal component as in an elliptical galaxy but also shows evidence of a flat disk-like structure as in the spiral galaxies.

Most galaxies are classified as 'normal', just like our own Galaxy. They appear to be aggregates of stars, evolving peacefully, except for the occasional supernova explosion, and their properties can be understood largely in terms of the evolution of their stellar populations. However, violent processes far more energetic than supernova explosions have been observed in the central regions of a few per cent of galaxies. Such phenomena have been

known since the early part of this century with the discovery of the optical jet in the giant elliptical galaxy M87 (Virgo A, 3C274), but the ubiquitous nature of such structures was appreciated only after the advent of radio astronomy. This led to the discovery of radio galaxies and quasars, which are powerful emitters of radio emission. High-resolution images of these objects made over the years have shown that they often exhibit radio jets, which are signatures of the beams carrying energy from the nucleus. Radio galaxies are associated with elliptical galaxies, and it appears that quasars with powerful radio emission, which constitute about 10 per cent of all quasars, also reside in host galaxies which are ellipticals. In addition to the jets, other signs of activity in the nuclear regions include rapid variability in the flux density, strong nuclear emission from stellar or semi-stellar nuclei, non-thermal emission from the nuclear regions, and strong emission lines with widths extending upto tens of thousands of km s^{-1}.

The zoo of active galaxies includes many different kinds of objects, the principal ones being the Seyfert galaxies, quasars, radio galaxies, BL Lac objects, starburst galaxies and the ultraluminous infrared galaxies. Sensitive searches have revealed evidence of nuclear activity in some of the so-called normal galaxies as well, and it is possible that all galaxies harbour an active nucleus or an AGN, but could be of much lower luminosity than the well-known active galaxies. Some of the different types of active galaxies are described briefly here.

Seyfert galaxies. Seyfert galaxies have a stellar or semi-stellar nuclei, are rich in strong, high-ionization emission lines, and are almost always found in spiral galaxies. Strong emission lines in the archetypal Seyfert galaxy NGC1068 was recognised as early as 1908, but the existence of this class of galaxies was first recognised by Carl Seyfert (1943). Spectroscopically, Seyfert galaxies are further classified into two main types. The type I Seyferts have narrow forbidden lines with widths of about several hundred km s^{-1} as well as broad permitted lines with widths extending up to about 10^4 km s^{-1}, while in type II Seyferts, only the narrow lines are seen.

Radio galaxies. These are powerful emitters of radio emission, and are associated with elliptical galaxies. Spectroscopically they are also classified into the narrow-line radio galaxies and the broad-line radio galaxies, analogous to the two types of Seyferts. Only about 5-10 per cent of luminous elliptical galaxies are powerful radio sources.

Quasars. Quasars are amongst the most distant and most luminous of all AGN. They have abnormally luminous nuclei, appear stellar on Palomar Observatory Sky Survey prints, are often variable and have a rich emission-line spectrum. Deep high-dynamic range observations from the ground as well as from the Hubble Space Telescope have shown that quasars reside in host galaxies which could be either spiral or elliptical (Clements & Pérez-Fournon 1997). Only about 5-10 per cent of quasars are strong radio sources and they appear to be associated with those whose host galaxies are elliptical.

BL Lac objects. These objects also have very luminous nuclei, are strongly variable, and are distinguished by the absence of strong emission and absorption features in their spectra. They are usually luminous radio sources.

A more detailed description of the properties of active galactic nuclei is beyond the scope of this thesis, but the range of radio luminosities of the different types of active galaxies is illustrated in Figure 1.1 (Condon 1988) and the X-ray luminosities of some of the different types of AGN and a normal galaxy for comparison are presented in Table 1.1 (Charles & Seward 1995).

Table 1.1. The X-ray luminosity of a few types of AGN

Type	L_x erg s^{-1}	Host galaxy	Example
Normal galaxy	10^{37} - 10^{39}	-	M31
Narrow emission line galaxy	10^{40} - 10^{43}	-	Mkn 176
Seyfert galaxy	10^{43} - 10^{45}	Spiral	NGC 4151
BL Lac objects	10^{44} - 10^{46}	Elliptical	OJ 287
QSOs	10^{45} - 10^{47}	?	3C273

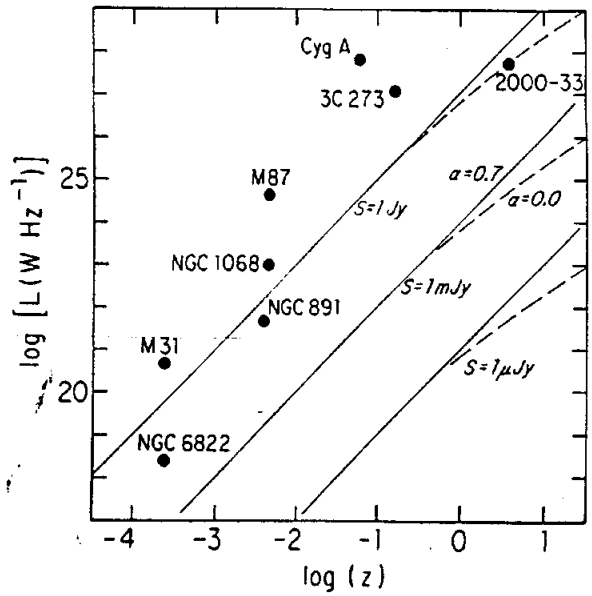

Fig. 1.1 The radio luminosity at 1.4 GHz versus redshift diagram for a representative sample of galaxies (Condon 1988). Towards the lower end of the luminosity range, NGC6822 is a dwarf irregular, M31 a normal typical spiral galaxy, NGC891 is a mild starburst galaxy and NGC1068 is the archetypal Seyfert 2 galaxy. At high radio luminosities the radio galaxies are associated with the elliptical galaxies. M87 is the well-known Fanaroff-Riley class I radio galaxy in the Virgo cluster, 3C273 and 2000-33 are associated with quasars while Cygnus A is amongst the most powerful radio galaxies.

1.1 Radio structures of radio galaxies and quasars

The radio structures of radio galaxies and quasars can be broadly described as consisting of two lobes of radio emission located more or less symmetrically on either side of the parent optical object, and a compact core or nuclear component coincident with the optical object. In addition, one often finds narrow collimated features called 'jets' connecting the core to the extended components, which are believed to be signatures of the beams carrying energy from the nucleus to the outer lobes. The overall linear sizes of radio sources range from less than a few tens of parsecs to over a few Mpc. The small sources with a steep high-frequency

radio spectrum are referred to as compact steep-spectrum objects, and are believed to be young objects which will later evolve into the larger sources.

The radio emission from the lobes as well as the nuclear component is believed to be due to synchrotron emission. The emission from the extended components has a steep radio spectrum ($\alpha > 0.5$, where the flux density $S \propto \nu^{-\alpha}$) and is optically thin, while the emission from the cores has a flat or complex spectrum and is optically thick to its own emission. The complex radio spectrum is due to a number of discrete components in the unresolved core (≤ 1 arcsec) which become self-absorbed at different frequencies due to synchrotron self absorption. High-resolution observations of the core by Very Long Baseline Interferometry techniques show that they themselves often have a core-jet structure with a number of knots or discrete features in the jet (Zensus & Pearson 1990; Zensus et al. 1995).

The extended radio emission from these objects can be classified into two categories, the Fanaroff-Riley class I and II types (Fanaroff & Riley 1974). The FRI sources are of lower luminosity, have diffuse extended plumes of emission, reasonably symmetric large-scale jets and are often brightest closer to the centre. The FRII sources are of higher luminosity ($P_{178} \geq 0.5 \times 10^{25}$ W Hz^{-1} sr^{-1} for H_0=100 km s^{-1} Mpc^{-1} and q_0=0), have prominent hot-spots at the outer edges which are identified with the regions where the energy-carrying beams interact with the external medium, and well-collimated, generally one-sided radio jets. Typical examples of an FRI and an FRII source are shown in Figure 1.2. The dividing luminosity between the two types appear to depend on the optical luminosity of the host galaxy (Zirbel & Baum 1995). The jets in FRII sources are believed to have higher Mach numbers and are less dissipative compared to the FRI sources. It has been speculated that the difference between the two types may be due to differences in the accretion rates onto the central black hole which may be the source of energy for these objects, as well as on environmental effects (Baum, Zirbel & O'Dea 1995).

Since the cores have a flat or complex spectrum while the extended emission has a steep

spectrum, the relative prominence of these features in the sources depends on the survey from which they have been selected. For example, sources chosen from the 3CR survey at 178 MHz or the Molonglo survey at 408 MHz will be dominated largely by the extended radio emission, while those from the S4 survey at 5000 MHz will have a much higher proportion of core-dominated, flat-spectrum objects.

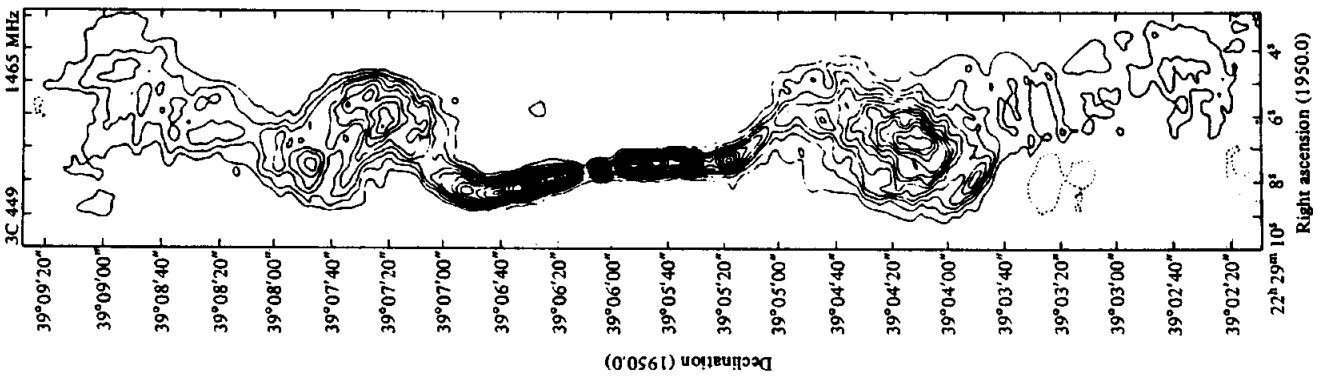

Fig 1.2(a) Radio image of 3C449, a typical FR I radio galaxy (Perley, Willis & Scott 1979).

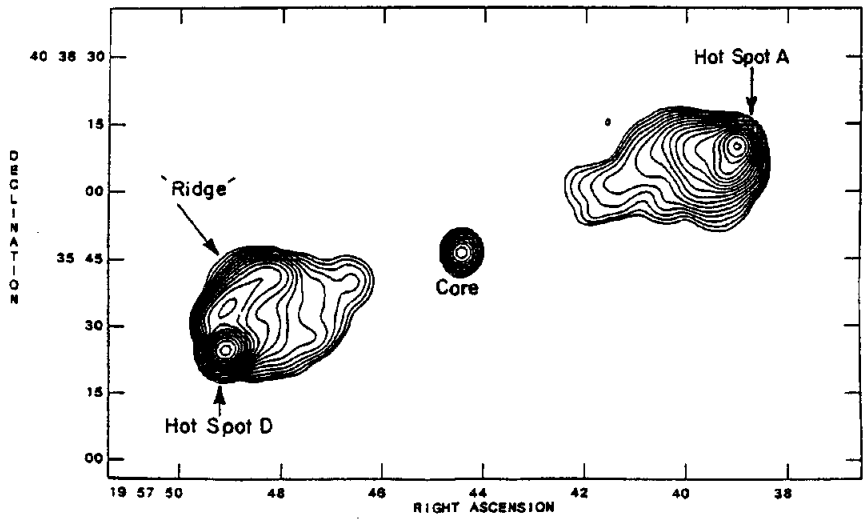

Fig. 1.2(b) Radio image of the well known FR II radio galaxy Cygnus A (Carilli et al. 1991).

1.2 Outflow pattern

The plasma containing mass, energy and magnetic fields, flows outwards in opposite directions from the nucleus to form the extended lobes of emission. The radio jets are the signatures of these energy-carrying beams, and as suggested by the observations, those associated with FRI sources are more dissipative along its path while in FRII sources the bulk of the energy is deposited in the hot-spots. Over the years, several models have been suggested to explain the double-lobed structure of radio sources, and one of the long-standing ones is the twin-exhaust model of Blandford & Rees (1974).

The Twin-Exhaust model. The active galactic nucleus is surrounded by dense thermal gas which may be flattened by rotation. The angular momentum defines an axis along which relativistic plasma generated in the nucleus flows outwards, and an equilibrium flow along this axis is established. The jet flows outwards via the formation of a de Laval nozzle (Figure 1.3). The jet velocity is sonic at a point where the cross-section is a minimum. The energy-momentum tensor of a portion of the fluid is given by $T_{ik} = wu_iu_k + pg_{ik}$ where $w = 4p$ (p is the pressure) is the enthalpy per unit proper volume of the fluid, $u_i = (\gamma, u, 0, 0)$ is the fluid 4-velocity ($\gamma = 1/(1 - \frac{v^2}{c^2})^{1/2}$ is the Lorentz factor) and g_{ik} is the flat space metric tensor. The momentum, energy and particle discharges are given respectively by $Q = (wu^2 + p)A$, $L = wu\gamma cA$, and $J = nuA$ (n is the particle number density and A is cross-sectional area of the jet). Assuming the flow to be isentropic and that there is no flow of particles across the walls, we get $\frac{w\gamma}{n} = constant$, since L and J are constants. Using the equation of state, $p = constant \times n^{4/3}$ we get, $p = p_0\gamma^{-4}$, where p_0 is the stagnation pressure when $\gamma = 1$ and $A = \frac{1}{4}Lp^{-3/4}{p_0}^{-1/4}[(p_0/p)^{1/2} - 1]^{-1/2}c^{-1}$. The cross-sectional area reaches a minimum of $3^{3/2}L/(8p_0c)$ when $p = p^* = 4/9p_0$. This corresponds to a bulk speed of $c/\sqrt{3}$. The radius of the jet assuming it to be of circular cross-section is $r = 2^{1/2}3^{-3/4}(p/p_0)^{-1/4}[1 - (p/p_0)^{1/2}]^{-1/4}r^*$.

The jet is susceptible to Rayleigh-Taylor and Kelvin-Helmholtz instabilities. The jet

impinges on the inter-galactic medium and the bulk kinetic energy is randomized at the shock where further mixing and particle acceleration may take place. The head of the jet is confined largely by the ram pressure of the inter-galactic medium(IGM) and the cocoon by the thermal pressure of the IGM in addition to any ram pressure due to transverse expansion of the lobes.

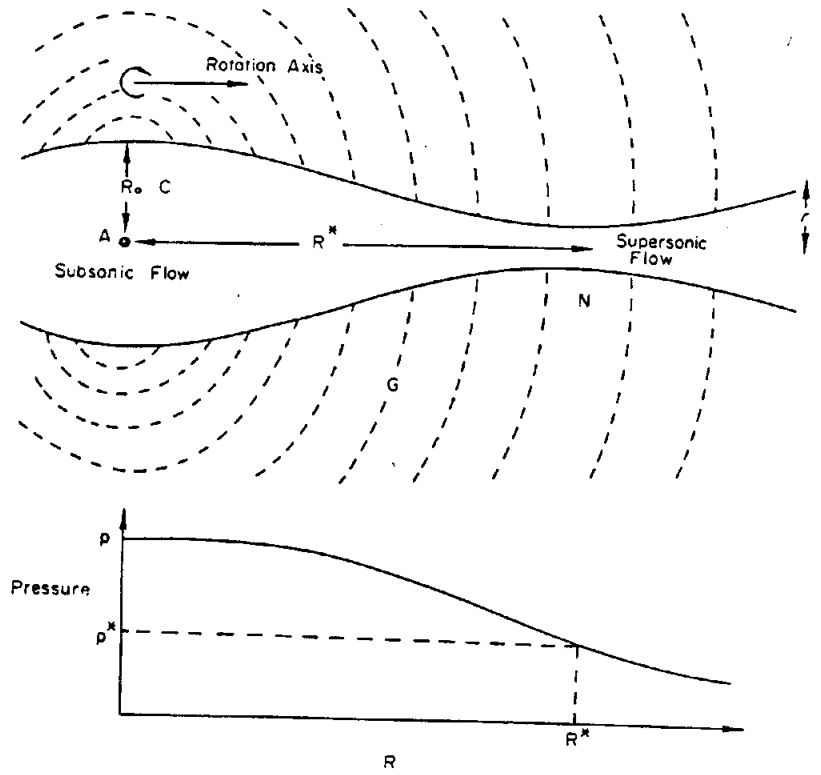

Fig. 1.3 A sketch of the de Laval nozzle in the twin-exhaust model, and the variation of pressure with distance R (Blandford & Rees 1974).

1.3 Spectral ageing and ages of radio sources

In a homogeneous, optically thin source with a constant magnetic field, a power-law continuum spectrum can be obtained if the relativistic electrons radiating by the synchrotron process has a power-law distribution, $N(E)dE = N_o E^{-p} dE$, where p, the slope of the power-law distribution of the energy of the radiating electrons is related to the spectral index α by $\alpha = (p-1)/2$. For a typical spectral index of 1, p=3.

Radio spectra often curve downwards at higher frequencies. The spectral index is about 0.75 at 1 GHz and about 1.25 at 9 GHz in the rest frame of the source for the high-luminosity 3CR sources (Mangalam & Gopal-Krishna 1995). This is because the electrons of energy E, radiate most of their energy at a frequency $\nu_c = 1.61 \times 10^7 B_\perp E^2_{GeV}$ MHz, where $B_\perp = Bsin\theta$ and θ is the pitch angle, the angle between the electron trajectory and the magnetic field. The rate of loss of energy, $-dE/dt$= A $B^2_\perp E^2_{GeV}$, which is proportional to the square of the energy. The constant A=6.08×10^{-9} when E is expressed in GeV and ν_c in MHz. Thus the highest energy electrons lose energy more rapidly and unless there is replenishment of the higher-energy electrons, the spectra will tend to curve downwards. In the twin-beam model for radio sources, the extended lobes of emission arise due to backflow from the hotspots as the beams advance outwards through the interstellar and then the intergalactic medium. Hence the radiating plasma closer to the nucleus would be older than that near the hotspot and one might find evidence of similar spectral ageing across the radio source. This can be used to estimate the ages of the lobes and possibly the velocity of advance of the hotspots if the distance to the source is known. Such studies have been done in the past (Burch 1977, 1979; Mayer 1979; Winter et al. 1980; Alexander et al. 1984; Myers & Spangler 1985; Alexander 1987; Alexander & Leahy 1987; Leahy, Muxlow & Stephens 1989; Carilli et al. 1991; Liu, Pooley & Riley 1992; Bridle et al. 1994), concentrating largely on sources from the 3CR sample.

1.4 Outline of this thesis

In this thesis we present the observations of 5 FRII radio galaxies selected from the Molonglo Reference Catalogue which are generally weaker than the 3CR sources, and examine any evidence of spectral index gradients in order to estimate their ages and velocity of advance of the hotspots. These observations were made with the Very Large Array (VLA) at the L-band with the hybrid CnB array and at the C-band with the BnA array. The thesis is organised as follows. In the next chapter (Chapter 2) we describe the basic physics of

energy-loss mechanisms, the spectral evolution of a radio source and estimates of their ages. In chapter 3 we present the details of observations and the analysis of the data. The results of our observations and the interpretation of these results are presented in Chapter 4.

Chapter 2

Spectral Index Evolution

Radio spectra of classical radio galaxies and quasars have in general no prominent sharp features, although the 21-cm line of neutral hydrogen, H_2O, CO, and OH transitions are detected in relatively nearby galaxies. The observations are thus confined mostly to the measurement of continuum spectra. The spectrum of 3C273 shown in Figure 2.1 is typical of a synchrotron-emitting source. The spectrum can be explained by radiation from individual electrons with power law energy distribution, $N(E) = kE^{-p}$, gyrating in a magnetic field **B** at relativistic speeds. The question one can ask is, does the spectrum change with time? The different processes that influence the evolution of the spectrum are related to the energy gains and losses of the radiating electrons, diffusion of electrons and injection of electrons.

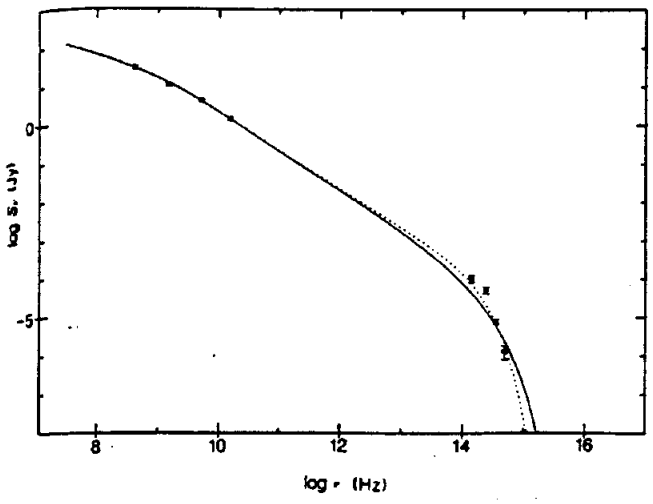

Fig. 2.1 Radio to optical spectrum of the hotspot of 3C273. The dotted curve shows the fit where the electron energy is cut off at $\gamma = \gamma_c = (320 \pm 30)[\frac{(1.5\pm0.6)GHz}{42Hz(B/1nT)}]^{1/2}$, while the solid curve shows the fit inferred from the Fermi acceleration model (Meisenheimer & Heavens 1986b).

2.1 Energy loss mechanisms for high energy electrons

Energy losses of the radiating electrons leads to changes in the energy spectra with time, and thus could potentially provide information about their life histories. The loss mechanisms involve interactions with matter, magnetic fields and radiation. These are discussed in detail in Longair (1994). The physical processes for the rate of energy loss due to different mechanisms are described briefly here.

2.1.1 **Ionisation losses.** The high energy electrons lose energy due to ionization of atoms and ions, the excitation of energetic atomic or ionic states, and production of Cherenkov radiation. The high energy particle interacts with atoms with a range of impact parameters 'b', resulting in a loss of kinetic energy. The upper limit to the impact parameter 'b_{max}' occurs when the duration of the collision is of the same order as the period of the electron orbit. There are two possibilities for the lower limit 'b_{min}', which occurs either (i) when the electrostatic potential energy of interaction is equal to the maximum possible energy transfer, or is (ii) dictated by Heisenberg's Uncertainty Principle of quantum physics. For the case of ionization of atomic hydrogen,

$$-(\frac{dE}{dt})_i = 7.64 \times 10^{-15} N(3ln\gamma + 19.8) \;\; eVs^{-1} \qquad (1)$$

where $\gamma = (1 - \frac{v^2}{c^2})^{-1/2}$ is the Lorentz factor of the electron, E is the energy of the electron and N is the number density of the hydrogen atoms in particles per cubic metre.

2.1.2 **Bremsstrahlung.** The acceleration of an ultrarelativisitic electron in the electrostatic fields of ions and the nuclei of atoms produce bremsstrahlung radiation. Following Heitler (1954), the energy loss rate for ultrarelativistic electrons can be written as

$$-\frac{1}{E}(\frac{dE}{dt})_{brems} = 4NZ^2{r_e}^2\alpha cg \qquad (2)$$

where r_e is the classical electron radius, Z is the atomic number, α is the fine structure constant and g is a Gaunt factor. The Gaunt factor takes two forms, viz., $g_1 = ln(2\gamma) - \frac{1}{3} =$

$ln\gamma + 0.36$ for nuclei unscreened as in fully ionized plasma, and $g_2 = ln(183z^{-1/3}) - 1/18$ for total screening. For fully ionized H-plasma, where it is appropriate to use g_1,

$$-\frac{1}{E}(\frac{dE}{dt})_{brems} = 7 \times 10^{-23} N(ln\gamma + 0.36)\ s^{-1}, \tag{3}$$

while for interaction between ultrarelativistic electron and neutral H-atom,

$$-\frac{1}{E}(\frac{dE}{dt})_{brems} = 3.66 \times 10^{-22} N\ s^{-1} \tag{4}$$

where the expression for g_2 is used. In both cases the rate of loss of energy is directly proportional to energy.

2.1.3 **Adiabatic losses.** As the volume of electrons expands against an external pressure 'p' it does work, given by pdV where dV is the change in volume, and hence loses energy. For an ultrarelativistic gas, loss due to expansion is given by

$$-(\frac{dE}{dt})_{ad} = \frac{1}{3}(\nabla.\mathbf{v})E \tag{5}$$

In the case of an uniformly expanding sphere of radius R, where the variation in velocity with distance from the centre, r, is $v(r) = v_0 r/R$. Here $v(r) = v_0$ at r=R.

$$-(\frac{dE}{dt})_{ad} = \frac{v_0}{R}E = \frac{1}{R}\frac{dR}{dt}E \tag{6}$$

$$-\frac{1}{E}(\frac{dE}{dt})_{ad} = \frac{1}{R}\frac{dR}{dt} \tag{7}$$

Adiabatic losses are important if the timescale of expansion $(\frac{1}{R}\frac{dR}{dt})^{-1}$ is similar to or faster than the time the particles have been within the emitting volume. This loss mechanism could be important for VLBI-scale knots and the lobes of radio sources, and particles escaping from supernova remnants.

2.1.4 **Synchrotron radiation.** The ultrarelativistic electron gyrating in a magnetic field radiates through the synchrotron process and produces non-thermal radiation. For ultrarelativistic electrons the energy loss rate is

$$-(\frac{dE}{dt})_{synch} = 2\sigma_T c\gamma^2 U_{mag} sin^2\theta, \tag{8}$$

where σ_T is the Thompson cross-section, U_{mag} is the magnetic energy density and θ is the pitch angle. This can be expressed as

$$-(\frac{dE}{dt})_{synch} = 1.587 \times 10^{-14}\gamma^2 B^2 sin^2\theta \ W = 9.9 \times 10^4 \gamma^2 B^2 sin^2\theta \ eV \ s^{-1}. \quad (9)$$

Averaging over an isotropic pitch angle distribution,

$$-(\frac{dE}{dt})_{synch} = \frac{4}{3}\sigma_T c\gamma^2 U_{mag} = 6.6 \times 10^4 \gamma^2 B^2 \ eV \ s^{-1} \quad (10)$$

2.1.5 **Inverse Compton scattering.** When an ultrarelativistic electron scatters a low energy photon the electron loses energy and the photon gains energy, which is re-radiated at a higher frequency. The energy loss rate for an ultrarelativistic electron by inverse Compton scattering in a radiation field of energy density U_{rad} is

$$-(\frac{dE}{dt})_{IC} = \frac{4}{3}\sigma_T c\gamma^2 U_{rad} \quad (11)$$

2.2 The diffusion-loss equation for high energy electrons

Let us consider the electrons in an energy interval (E, E+dE) and a space interval (x, x+dx), as shown in Figure 2.2. This can be generalized to three spatial coordinates. The number of particles in the cell shown is N(E,x,t)dEdx. The rate of change of particle density in this cell is

$\frac{d}{dt}N(E,x,t)dEdx = [\phi_x(E,x,t) - \phi_{x+dx}(E,x+dx,t)]dE + [\phi_E(E,x,t) - \phi_{E+dE}(E+dE,x,t)]dx + Q(E,x,t)dEdx$

where Q(E,x,t) is the rate of production of electrons per unit volume of coordinate space, and ϕ is the flux of electrons.

Taylor expanding,

$$\frac{dN}{dt} = -\frac{\partial \phi_x}{\partial x} - \frac{\partial \phi_E}{\partial E} + Q = D\frac{\partial^2 N}{\partial x^2} - \frac{\partial \phi_E}{\partial E} + Q; \ since \ \phi_x = -D\frac{\partial N}{\partial x} \quad (12)$$

where D is the diffusion constant.

Generalising this to three spatial coordinates,

$$\frac{dN}{dt} = D\nabla^2 N - \frac{\partial \phi_E}{\partial E} + Q = D\nabla^2 N + \frac{\partial}{\partial E}[b(E)N(E)] + Q(E,t)\,;\; N(E)\frac{dE}{dt} = \phi_E = -b(E)N(E) \tag{13}$$

If only synchrotron losses are considered and if the electron distribution is uniform spatially then,

$$\frac{dN}{dt} = -AB_\perp^2 \frac{\partial}{\partial E}[E^2 N(E)] + Q(E,t) \tag{14}$$

where A is a constant which is equal to 6.08×10^{-9} when E is in GeV and ν_c is in MHz, as discussed in chapter 1.

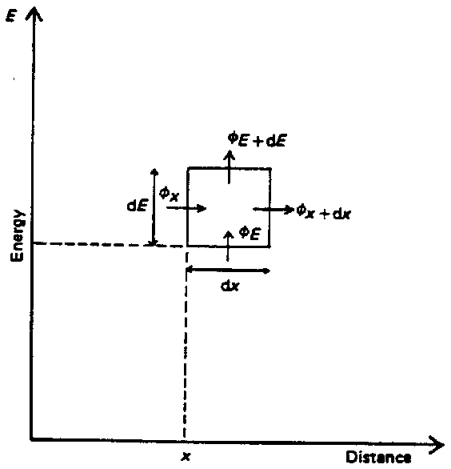

Fig. 2.2 Energy-Spatial coordinate diagram used in deriving the diffusion equation.

2.2.1 Instantaneous injection. For the initial energy distribution at time t=0 being,

$$N(E,0)dE = kE^{-p}dE \quad for\ E_1 < E < E_2 \tag{15}$$

and zero at other energies, and if $Q(E,t) = 0$, then after time t,

$$N(E,t)dE = \frac{kE^{-p}dE}{(1 - AB_\perp^2 Et)^{2-p}} \quad for\ E_1' < E < E_2' \tag{16}$$

and zero at other energies, where $E' = E/(1+AB_\perp^2 Et)$. Even for an initial energy distribution extending to an infinite energy, we will have a cutoff at $E_c = 1/AB_\perp^2 t$ at time t.

The evolution of spectrum is as shown in Figure 2.3. The synchrotron radiation spectrum is a power law, $S \propto \nu^{-\alpha}$. The upper cutoff frequency is $\nu_c \approx 1000 B_{\perp,gauss}^{-3} t_{years}^{-2} MHz$. For

frequencies $\nu < \nu_c$ the radiation losses are not important and $\alpha = (p-1)/2 \equiv \alpha_0$. For frequencies $\nu > \nu_c$ the spectral index is $\alpha = -(2p+1)/3 = (\frac{4}{3}\alpha_0 + 1)$ (Kardashev 1962).

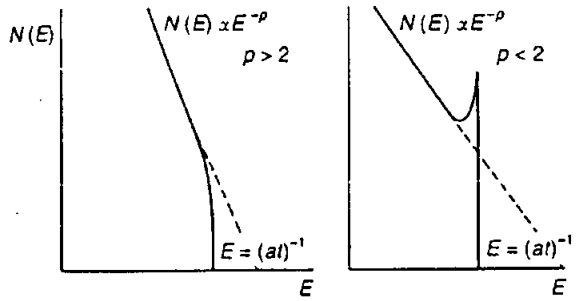

Fig. 2.3 The evolution of a power-law energy spectrum for cases p greater and less than 2, for electrons injected at t=0 with no subsequent injection (Longair 1994).

2.2.2 Continuous injection. When there is continuous supply of relativistic electrons the equilibrium solution is given as,

$$N(E) = \frac{K}{p_0 + 1} \frac{E^{1-p}}{AB_\perp^2 E^2} \tag{17}$$

Figure 2.4 shows the energy spectrum. For frequencies $\nu > \nu_c$ the rate of energy lost as radiation is equal to that gained by addition of new electrons and the spectral index is $\alpha_0 + \frac{1}{2}$. Below this frequency the radiation losses are not important and the spectral index is α_0.

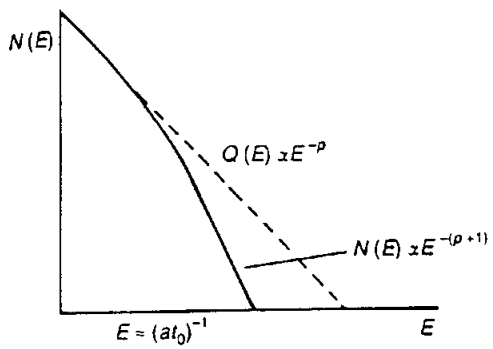

Fig. 2.4 The solution of continuous injection of electrons with power-law energy spectrum (Longair 1994).

2.2.3 Recurring injection. For injection of particles through a series of recurring injections, the radiation spectrum will vary with time in the following manner: at time t after the first injection of electrons, the radiation losses will not be important for $\nu < 1000B_{\perp}^{-3}t^{-2}$ and the spectral index is equal to the initial value. For frequencies $1000B_{\perp}^{-3}t^{-2} < \nu < 1000B_{\perp}^{-3}T^{-2}$, where time scale for energy loss is longer than the period T between bursts, the injection can be considered quasi-continuous. Radiation losses are balanced by injection of new electrons, and the spectral index is $\alpha_0 + \frac{1}{2}$. For frequencies $\nu > 1000B_{\perp}^{-3}T^{-2}$ the rate of injection is not sufficient to balance the radiation losses and the spectrum steepens to $(\frac{4}{3}\alpha_0 + 1)$. The time evolution of the spectrum is shown in Figure 2.5.

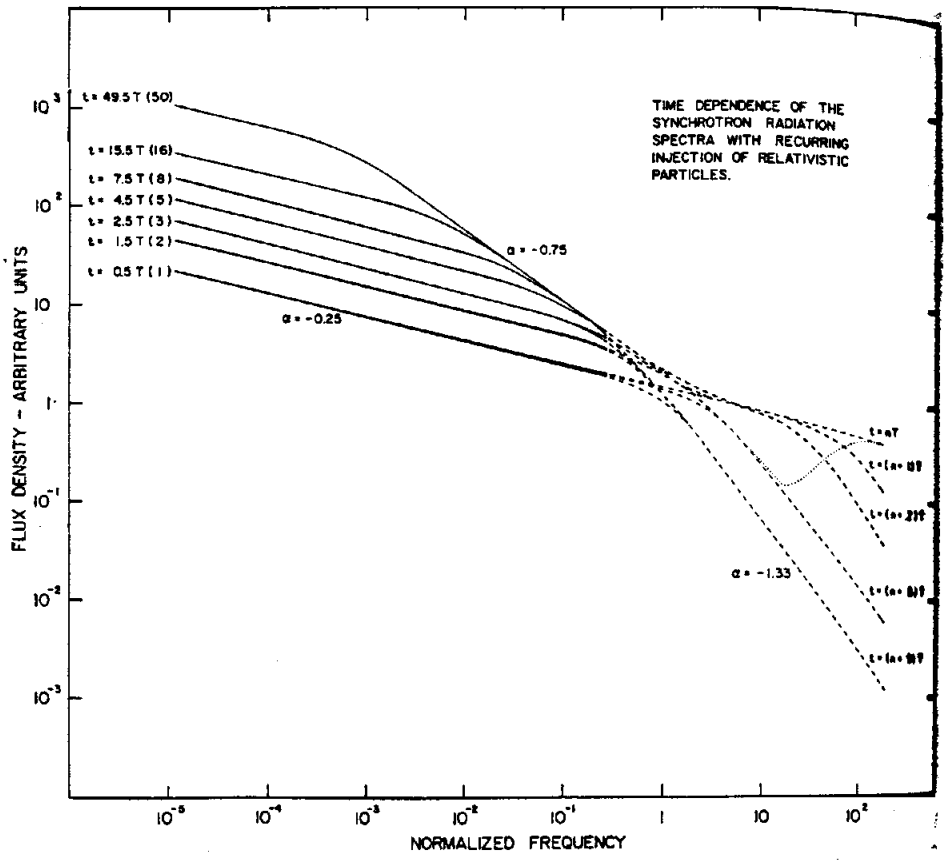

Fig. 2.5 The evolution of the frequency spectrum for an initial injection spectrum N(E)=K $E^{-1.5}$, and recurring injection of electrons occurring at regular time intervals 'T' (Kellermann 1966).

2.3 Indicators of Age

The energy spectrum of synchrotron-emitting electrons evolve with time. So it is possible to make an estimate of the time since the electrons were last accelerated. As discussed earlier, the lobes of radio sources represent backflow from the hotspots where they were last accelerated. Hence the electron populations of different ages occupy different spatial positions in a radio source, which can be studied from high-resolution spectral-index images of these sources. The development of interferometric techniques paves the way for such a work by providing sufficient beamwidths across the source at significantly different wavelengths. The expression for electron age is obtained using the following assumptions:

1. the magnetic flux density of the source (B) is constant throughout the source;
2. the spectrum of initial electron injection is $N(E)dE = N_0 E^{-p} dE$;
3. the electrons are isotropized on time-scales short compared with radiation time-scales (Jaffe & Perola 1973).

The synchrotron losses are better reflected in the 2-frequency spectral index images rather than the total-intensity ones. The total intensity changes with thickness of the source and it is more sensitive to expansion losses. Considering only the synchrotron losses, the electron energy spectrum is given by (Pacholczyk 1970),

$$N(E,\theta,t) = N_0 E^{-p}[1 - C_2 B^2 sin^2\theta E t]^{p-2} \tag{18}$$

The intensity of synchrotron radiation is,

$$I_\nu = 4\pi C_3 N_0 s B \int_0^{\pi/2} d\theta sin^2\theta \int_0^{E_T} dE F(x) E^{-p}[1 - C_2 B^2 < sin^2\theta > E t]^{p-2} \tag{19}$$

where s is the thickness of the source, $E_T = [C_2 B^2 sin^2\theta t]^{-1}$ and $x = \nu/\nu_c$. The total intensity depends on the frequency, magnetic field and time.

$$I_\nu = f(\nu, B, t) \tag{20}$$

$$I_\nu / I_0 = f(X_0) \;\; ; \;\; X_0 = (C_2{}^2/C_1)\nu B^3 t^2 < sin^2\theta >^2 \;\; and \;\; I_0 = I_\nu(t=0) \tag{21}$$

In these equations C_1, C_2 and C_3 are constants defined by Pacholczyk (1970). Their values are 6.27×10^{18}, 2.37×10^{-3} and 1.87×10^{-23} respectively in the cgs units.

From the above equations a relation between a 2-frequency spectral index and X_0 can be obtained (Myers & Spangler 1985).

$$\alpha_{4.9}^{1.4} = g(X_0) \tag{22}$$

The age of the radiating electrons at a given point is found using the 2-frequency spectral index, calculated value of equipartition magnetic field and frequency of observation. The equipartition magnetic field is calculated using

$$B_{min} = [\frac{3\mu_0}{2} \frac{G(\alpha)\eta L_\nu}{V}]^{\frac{2}{7}} \tag{23}$$

obtained by minimising the total energy, which corresponds to the approximate equality of the energies in relativistic particles and magnetic field. $G(\alpha)$ is a constant which weakly depends on the spectral index α and the frequency range over which the source radiates. We have used α= 0.9 and frequency range as 10 MHz to 10 GHz. μ_0 is the magnetic permeability constant for vacuum, V is the volume and L_ν is the luminosity of the source. We have taken η, the ratio of total energy of the particles to the energy of the electrons, to be unity, thus neglecting the energies of protons and heavier nuclei. The distance of the source is found using the cosmological model, $q_0 = 0$ and $H_0 = 100\ kms^{-1}Mpc^{-1}$.

The electron age can also be found out using the break frequency ν_T of the spectrum,

$$t = [\frac{9C_1 B}{4{C_2}^2(B^2 + B_{MWB}^2)^2 \nu_T}]^{1/2} \tag{24}$$

where C_1 and C_2 are constants defined by Pacholczyk (1970) and $B_{MWB} = 0.32(1+z)^2$ nT is the equivalent magnetic field strength of the cosmic microwave background radiation. The spectral index is $\alpha_0 = (p-1)/2$ below the break frequency and above which the spectrum steepens. For observations of three or more frequencies, the break frequency is derived by fitting a theoretical spectrum to the observed one.

2.4 Models for the evolution of the electrons

The three models for the evolution of the energy spectrum of the electrons with time, which are often discussed in the literature (cf. Carilli et al. 1991), are the Continuous Injection(CI), Kardashev-Pacholczyk(KP), and Jaffe-Perola(JP) models. The initial spectrum is assumed to be a power-law in energy, and isotropic in pitch angle, and the magnetic field is assumed to be isotropically tangled on scales smaller than the resolution. The spectral break frequency above which the spectrum steepens from the initial power law is related to the magnetic field, B, (equation 24) and the synchrotron age is the time since the energy spectrum had a single power law to 'infinite' frequency. However, the models predict different forms of the high-frequency fall-off. In the JP and KP models, there is a one-time injection of the power-law distribution of electrons. The KP model assumes that the pitch-angle of an individual electron is constant, but the pitch-angle is different for different electrons. The electron whose motion is perpendicular to the field loses energy faster compared to an electron travelling almost parallel to the field. This model does not allow for pitch angle scattering of the relativistic particles, and there is a population of high-energy particles at oblique pitch angles. In the JP model, the pitch-angle of an individual electron is rapidly isotropized, leading to a sharper break in the energy spectrum. The pitch angles are scattered on time scales much smaller than the radiative life times of the electrons. In the CI model, there is a continuous injection of relativistic electrons with the same power law distribution in energy. This model was initially applied to sources which were unresolved so that all the radiating particles are observed at any given time. At low-frequencies below the break frequency, one would observe an increase in the flux density with time since new particles are being continuously injected. Above the break frequency, the spectrum is influenced by the injection of new particles and the falloff is more gradual that either the JP or KP models, the increase in spectral index being 0.5. For well-resolved sources, the CI models are applicable when there is continuous injection of particles via for example shocks, in a region within the telescope beam. A steady state where the break frequency is the same can be

obtained if there is also outflow of radiating particles from the region within the telescope beam (Heavens & Meisenheimer 1987; Meisenheimer et al. 1989).

In multifrequency observations of radio sources, a sharp break in the frequency spectrum is not usually observed. For example in Cygnus A, the observations could be fitted by the KP model but not the JP model (Carilli et al. 1991). In the conventional approach, one assumes the field strength to be a constant. Tribble (1993) considers the ageing of synchrotron electrons in a random magnetic field, where the magnetic field is described by a Gaussian random field. The break frequency depends upon the magnetic field strength, and there is a range in break frequency corresponding to the range in magnetic field strength. As a result, the sharp break in the spectrum given by the JP model is not seen, and the spectrum is similar to that of the KP model. In realistic scenarios, it is reasonable to assume that electrons are scattered in pitch angle, and the absence of a sharp break could be due to scattering of pitch angles, more realistic magnetic field configurations and diffusion of electrons between regions of different field strengths. There are other possibilities as well which could smear the break in the spectrum.. Alexander (1987) explains the lack of a spectral index gradient in the western lobe of 3C234 by invoking reacceleration mechanisms. The same observations are explained by Wiita & Gopal-Krishna (1990) by assuming a large-scale magnetic field gradient along the source axis.

2.5 Difficulties in real sources

There are effects which should be included, or at least borne in mind, in more realistic models of the evolution of the spectra of radio sources. Some of these are as follows.

Expansion losses. These lead to a reduction in particle energy and the magnetic field strength. The spectrum scales to lower frequencies and lower values of flux density (cf. Scheuer & Williams 1968). While synchrotron losses have little effect on the flux density below the break frequency, expansion losses lead to a significant decrease in the flux density.

Particle reacceleration. Particle reacceleration changes the energy distribution. This

may affect only the high energies, decreasing the degree of spectral steepening of the entire spectrum (cf. Kardashev 1962).

Inverse Compton scattering. Inverse Compton scattering with the cosmic microwave background radiation, can be an important factor particularly for sources at large redshifts.

Geometrical effects. If the source is not in the plane of the sky, a line of sight through the source will intercept regions of different ages.

Magnetic fields. The magnetic fields may change along the source axes, and it may be incorrect to use a global average value.

Electron energy distribution. It has been assumed that the electron injection spectrum has a power law, based on the observation that the integrated spectra of radio sources can usually be explained by a power-law distribution in electron energies.

Chapter 3

Observations and analysis

To study spectral index gradients across the lobes of radio sources, one ideally needs observations with similar resolutions at a number of frequencies. Also, the sources should be observed with at least about 10 to 15 beamwidths across the source to identify any possible gradients in the spectral index.

3.1 Sample of sources

In this study we have selected five high-luminosity Fanaroff-Riley class II sources from the Molonglo Reference Catalogue (MRC), complete to 1 Jy at 408 MHz (Large et al. 1981). They were chosen such that they have a large angular size, having at least about 10 beamwidths across the source axis, and significant emission from the lobe in the available images. The sources are listed in Table 3.1 which is self explanatory. Their angular sizes range from about 60 to 140 arcsec, giving us about 10 to 30 beamwidths across the source axes with a resolution of about 5 to 6 arcsec.

Table 3.1 Observational details

Source Name	Opt.[a] Id.	Opt. Posn. [a] RA DEC	S^{b}_{178MHz} Jy	z[a]	log P_{178MHz} $WHz^{-1}sr^{-1}$	LAS[c] "	l[c] kpc
0148-297	G	01 48 19.59 -29 46 46.3	15.298	0.410	26.48	141.5	511.4
0428-281	G	04 28 16.98 -28 07 12.4	4.979	0.650	26.47	62.1	285.7
1126-290	G	11 26 25.72 -29 05 01.7	4.934	0.410	25.98	104.1	376.2
2325-213	G	23 25 58.08 -21 22 22.6	6.868	0.580	26.51	82.1	357.9
2348-235	G	23 48 53.26 -23 33 47.3	3.012	0.952	26.67	62.7	336.3

a- from McCarthy et al. (1996)

b- by extrapolating the fluxes at other frequencies available in Wright et al. (1990)

c- from 1365 MHz observations of this thesis. We assume H_0=100 km s^{-1} Mpc^{-1}, q_0=0.

3.2 Observations

The observations were made with the Very Large Array (VLA) on 1995 September 21 at 1365 MHz using the BnA array, on 1996 January 20 at 4635 MHz for four sources, and on 1996 January 31 at 4635 MHz for the source 1126-290 using the CnB array. Since it is desirable to have similar resolution at both the frequencies, the observations were made with different arrays, each yielding a resolution of about 5 to 6 arcsec at both frequencies. Also, since the sources are in the southern hemisphere, the observations were made with a hybrid array to get a roughly circular beam.

The primary flux density calibrators were 3C286 for the L-band, and 3C286 and 3C48 for the C-band observations. The flux densities of these primary calibrators are calculated using the parameters A, B, C and D given in Perley & Taylor (1996), in the AIPS task *setjy*. The secondary calibrators used were 0237-233, 0454-234, 1110-217 and 2331-240 for the L-band, and 0202-172, 0454-234, 1124-186 and 2331-240 for the C-band observations.

3.3 Calibration of the data

Data analyses including calibration and making the final images was done using the Astronomical Image Processing System (AIPS) developed by the National Radio Astronomy Observatory (NRAO). Initial editing of the data were done using the AIPS tasks *quack*, which flags the bad points at the beginning of each scan on a source, and *tvflg*, which enables one to interactively edit bad amplitudes and phases. The flux density of the primary calibrators was set using *setjy*, and the task *vlacalib* was run for the calibrators to produce an SN or solution table containing antenna-based gain corrections. Further editing of the data was done after examining the solutions, and the task was rerun. Then the flux density of the phase calibrators was set using the task *getjy*, and the task *vlaclcal* was run to calibrate the antenna gains and interpolate it into a calibration or CL table. The data was checked to ensure that calibration was satisfactory before making the images. The flux densities

estimated for the secondary calibrators are listed in Table 3.2.

Table 3.2 Fluxes of the calibrators used

Calibrator Name	Observing Date	S_{1365} Jy	S_{4635} Jy
1328+307	21-SEP-1995	15.04*	
2331-240	21-SEP-1995	0.81	
0237-233	21-SEP-1995	6.38	
0454-234	21-SEP-1995	1.36	
1110-217	21-SEP-1995	1.50	
0134+329	20-JAN-1996		5.77*
0202-172	20-JAN-1996		1.35
2331-240	20-JAN-1996		0.83
0454-234	20-JAN-1996		1.24
1328+307	31-JAN-1996		7.71*
1124-186	31-JAN-1996		0.96

*calculated using the parameters A, B, C and D given in Perley & Taylor (1996)

3.4 Imaging

The initial maps were made using the task *imagr* with a cell size of 1 arcsec and and an image size of 512 × 512 pixels. The clean components from this initial map were combined using the task *ccmrg*, and the data were self-calibrated using the clean components from the source. Self-calibration was done (task *calib*) initially to correct the phases and later to correct the amplitudes as well as the phases. The images at both frequencies were made with the same circular beam of 5-6 arcsec, have same cell size and image size. The positions of the pixels at the corners of the maps were compared to ensure that they correspond to the same position in space. The images at the two frequencies were combined to produce a spectral index map between 1365 and 4635 MHz using the task *comb*.

The errors in the flux density propagate to the calculated age through the spectral index.

Two possible errors in the flux density are the random noise error which is the noise level in the maps and an assumed error of 5% for any systematic errors.

For a power-law spectrum, the flux density (S) is related to the frequency ν as, $S \propto \nu^{-\alpha}$. The spectral-index α can be calculated using flux density measurements at two different frequencies as, $-\alpha = \frac{logS_1/S_2}{log\nu_1/\nu_2}$. The error in the spectral index is related to the errors in flux density measurements at two frequencies, assuming that there is no error in the frequencies as, $\sigma_\alpha^2 \approx \sigma_{S_1}^2(\frac{\partial\alpha}{\partial S_1})^2 + \sigma_{S_2}^2(\frac{\partial\alpha}{\partial S_2})^2 = \sigma_{S_1}^2(\frac{1}{S_1 log\nu_1/\nu_2})^2 + \sigma_{S_2}^2(\frac{1}{S_2 log\nu_1/\nu_2})^2$. Now, $\sigma_{S_1}^2 = (\frac{5}{100}S_1)^2 + (map\ noise_1)^2$, using 5% error in flux density for systematic errors. The error in spectral index is, $\sigma_\alpha^2 \approx 2(\frac{5}{100}\frac{1}{log\nu_1/\nu_2})^2 + \frac{1}{(log\nu_1/\nu_2)^2}[(\frac{map\ noise_1}{S_1})^2 + (\frac{map\ noise_2}{S_2})^2] = 0.0177 + 3.548[(\frac{map\ noise_1}{S_1})^2 + (\frac{map\ noise_2}{S_2})^2]$.

The noise and flux densities are per beam values. The error in the spectral-index increases as the flux density per beam decreases as one moves away from the hotspots towards the central region. The variation in the error bar of the spectral index as a function of signal to noise ratio is shown in Table 3.3. The spectral index gradient plot is obtained only at regions where the flux density is well above of the noise. The regions where signal to noise ratio is less than 10σ is clipped. The typical value of the error in the spectral index is around 0.14 at the hotspots and 0.30 at the lobes farthest away from hotspots.

Table 3.3 Variation of the error in the spectral index, σ_α, with signal to noise ratio

S/map noise	σ_α
3	0.898
5	0.549
10	0.298
15	0.222
20	0.188
25	0.170
50	0.143
100	0.136
∞	0.133

Chapter 4

Spectral ageing and concluding remarks

In the standard model of extragalactic radio sources, the hotspots represent the regions where the beams interact with the external medium, and where the flow from the nucleus is shocked and energy is dissipated. The radio-emitting material from the lobes represents outflow from the hotspots. Thus the electrons radiating in the lobes are older than those in the hotspots, and accordingly the radio spectra of the powerful radio sources steepen as one goes away from the hotspots to the edges of the lobes near the core. In this chapter we present the results of our study of the spectral morphology of five radio galaxies. We first present the images of our sample of sources, and then examine the variation in spectral index across the lobes of these sources.

4.1 Observational results

The images of all the five radio galaxies at 1365 and 4635 MHz with an angular resolution of about 5 arcsec, the spectral index images with the same resolution, and the integrated spectra of the sources using values from NASA Extragalactic Database (NED) as well as from our measurements, are presented in Figures a of 4.1 to 4.5. Table 4.1 presents the total flux density and rms noise in the maps of the sources at 1365 MHz and 4635 MHz, and the Half Power Beam Width (HPBW). The difference in the flux density in the C-band image as compared to that interpolated by fitting a least-squares straight line fit to the data available in the catalogue (NED) has been estimated for our sources. These values are 57 mJy for 0148-297, 32 mJy for 0428-281, 61 mJy for 1126-290, 6 mJy for 2325-213 and 27 mJy for 2348-235, with the interpolated values being larger than our measurements. The measured values are lower by 6.6%, 11.4%, 19.7%, 2.1% and 19.3% of their C-band flux densities respectively for each of the above sources. Since the number of available measurements are

few and could also be significantly affected by confusion, the detailed spectral shape of the integrated spectrum is not well determined and the listed values of the missing flux density could have significant uncertainties. Weak, extended features seen in the $\lambda 20$ cm images are often not well represented in the $\lambda 6$ cm images. However, our estimates of spectral index variation are from scaled-array observations, and are confined to regions of high signal to noise ratios, and should not be significantly affected by any possible missing flux density. The positions and flux densities of the individual components are listed in Table 4.2, which is arranged as follows. Column 1: source name; column 2: identification of the component; columns 3 and 4: the right asension and declination in 1950 co-ordinates of the pixel of maximum brightness; columns 5 and 6: the peak and integrated flux density at 1365 MHz; columns 7 and 8: the peak and integrated flux density at 4635 MHz.

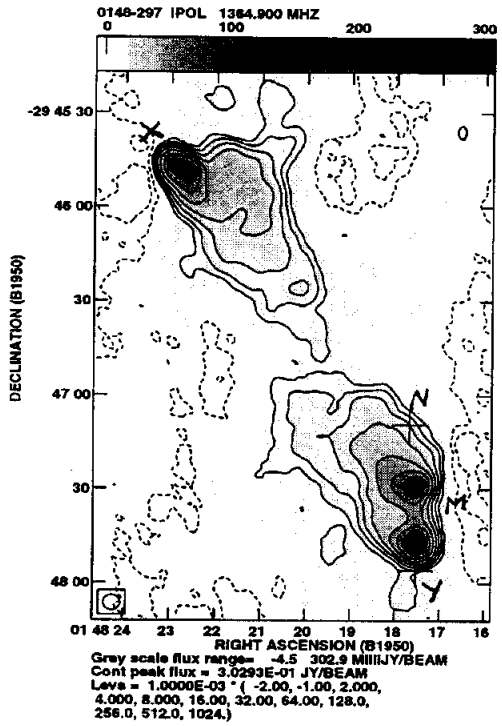

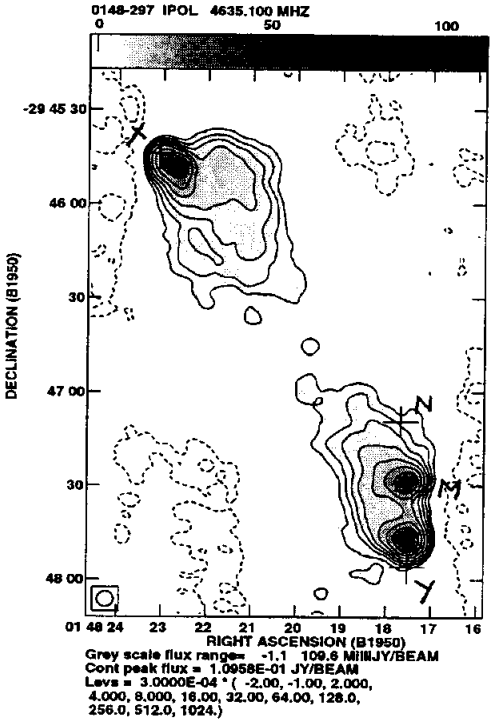

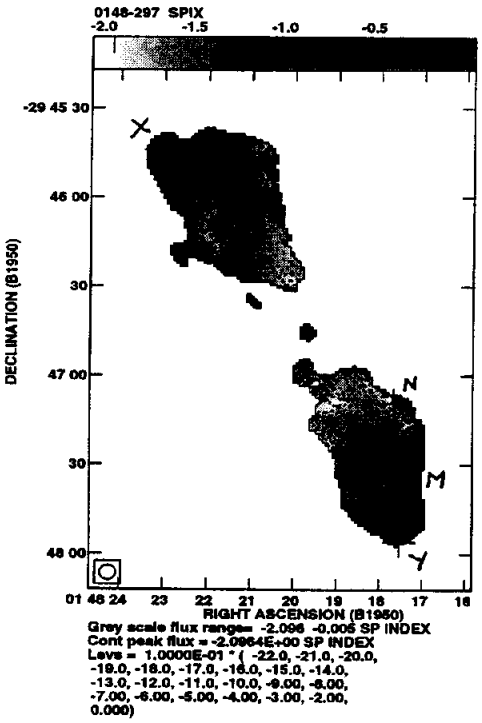

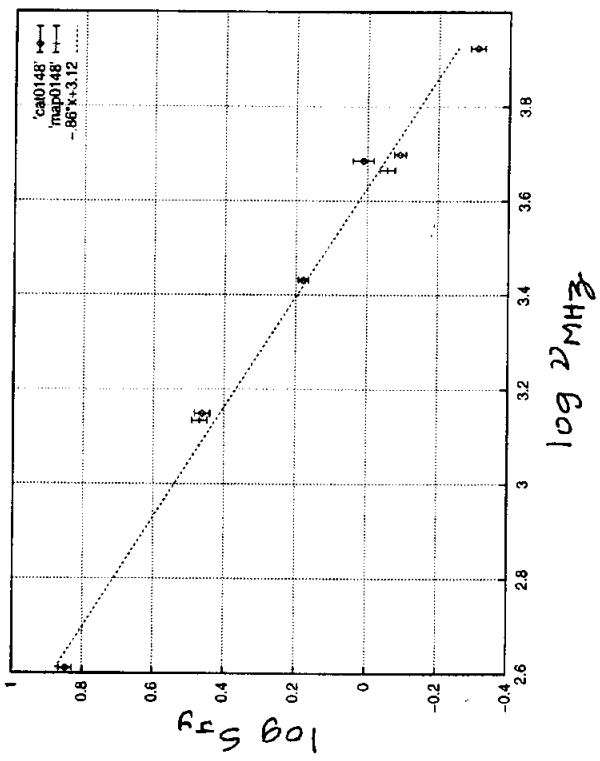

Fig. 4.1a. The L-band, C-band and spectral-index maps of 0148-297, and the radio spectrum obtained from low-resolution measurements in the literature. The straight line represents the linear least squares fit to these points which are represented by ○. The total flux densities estimated from our images are marked with a −.

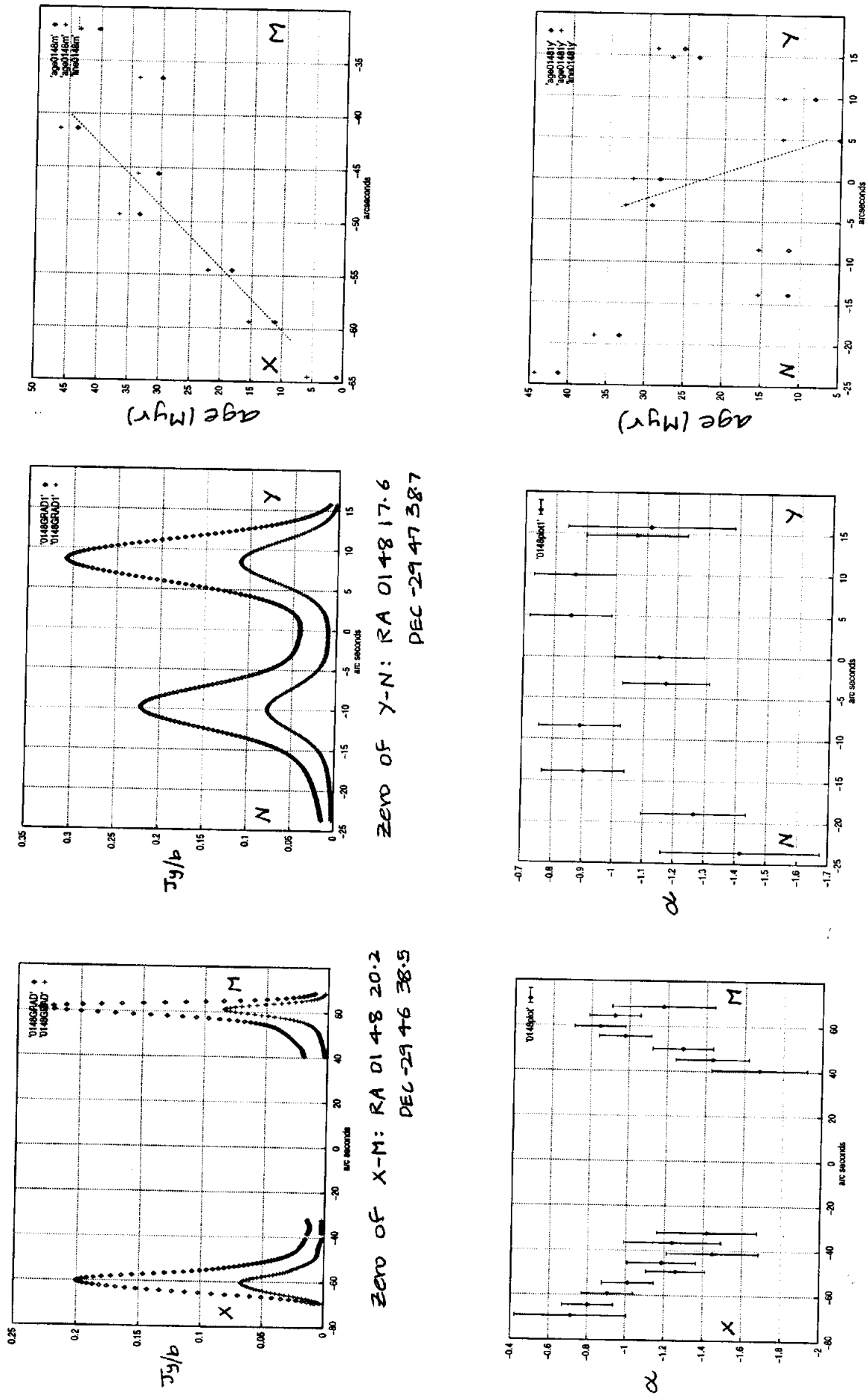

Fig. 4.1b The total intensity in L(∘) and C(+) bands, spectral-index, and age (∘ using the determined hotspot spectral-index and + using 0.75 as hotspot spectral-index) gradients along the chosen axes of 0148-297, which are marked in Fig. 4.1a.

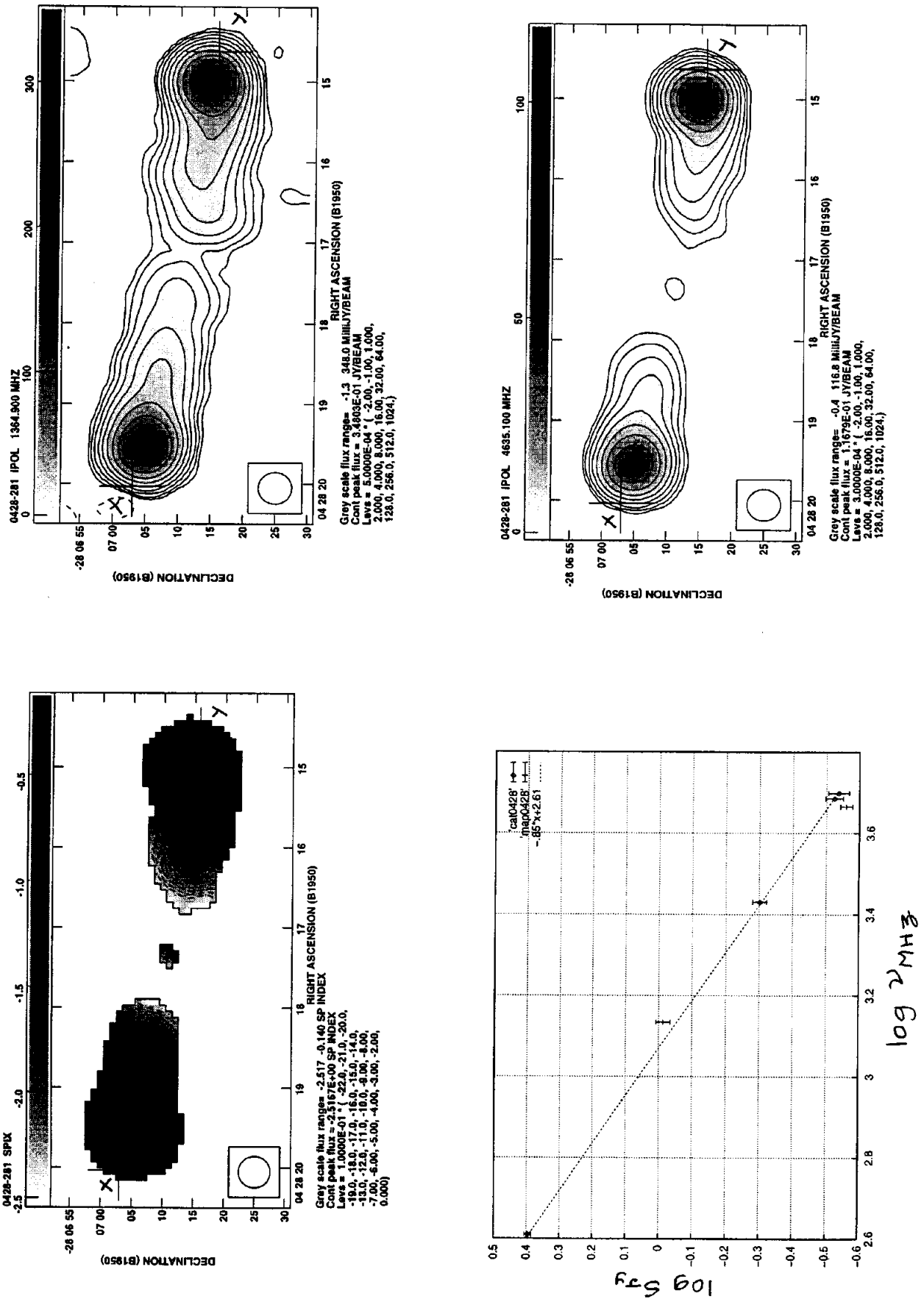

Fig. 4.2a. The L-band, C-band and spectral-index maps of 0428-281, and the radio spectrum obtained from low-resolution measurements in the literature. The straight line represents the linear least squares fit to these points which are represented by ◇. The total flux densities estimated from our images are marked with a −.

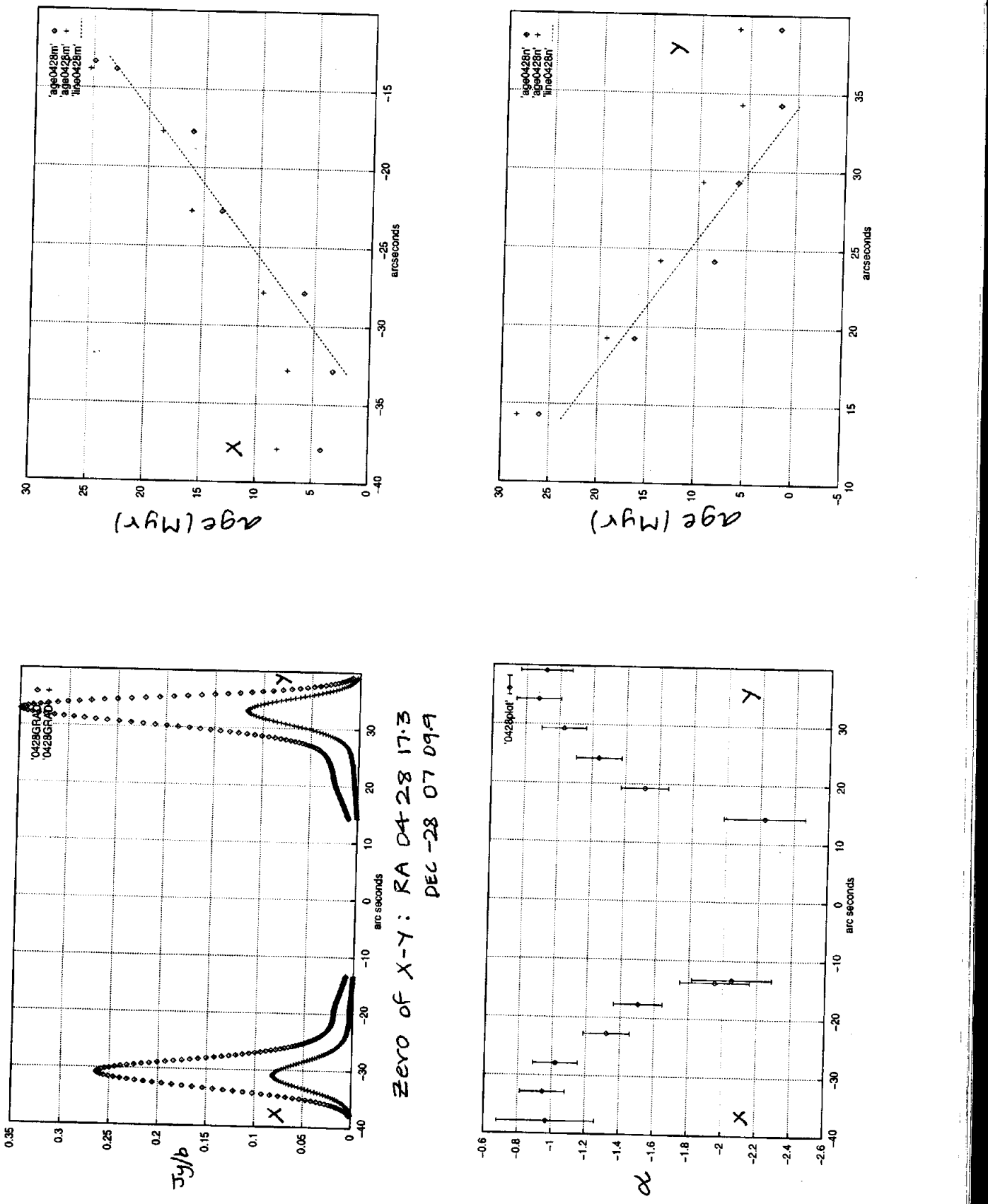

Fig. 4.2b The total intensity in L(⋄) and C(+) bands, spectral-index, and age (⋄ using the determined hotspot spectral-index and + using 0.75 as hotspot spectral-index) gradients along the chosen axis of 0428-281, which are marked in Fig. 4.2a.

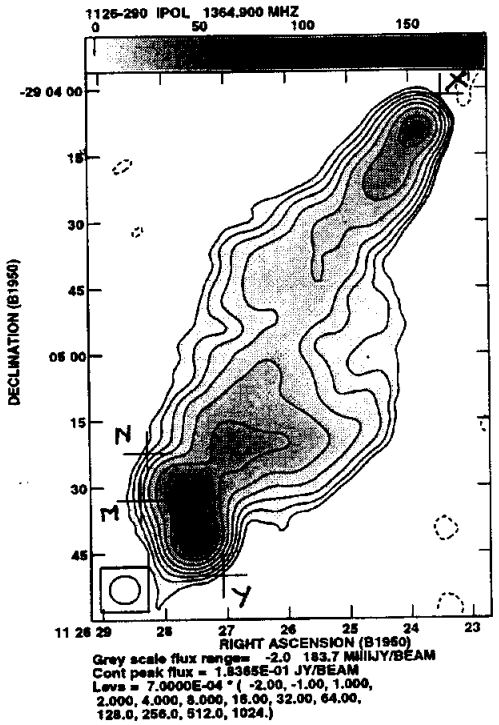

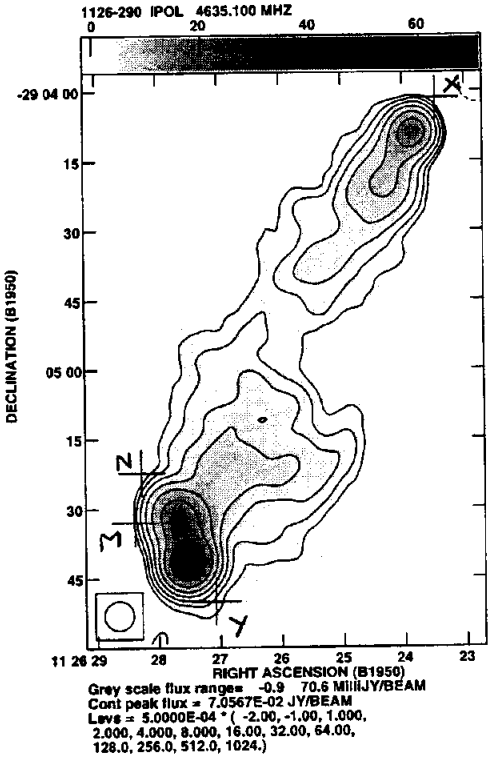

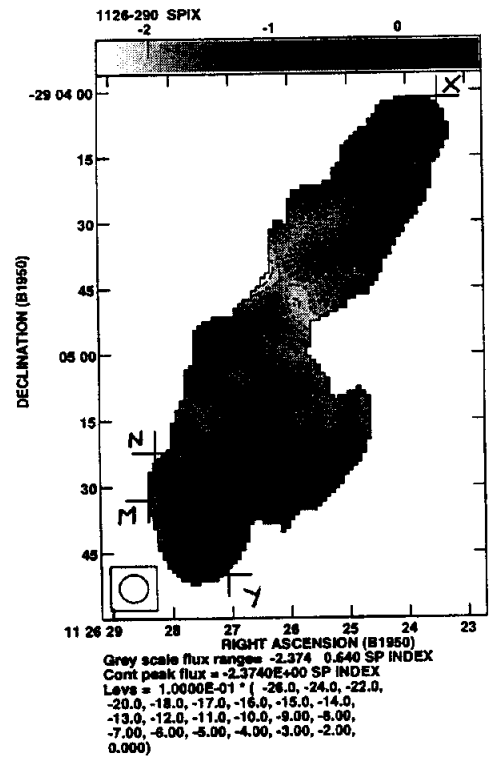

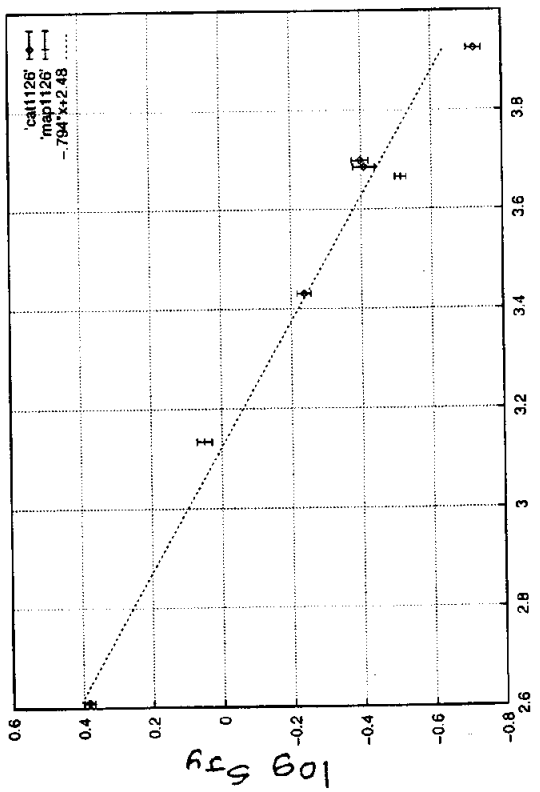

Fig. 4.3a. The L-band, C-band and spectral-index maps of 1126-290, and the radio spectrum obtained from low-resolution measurements in the literature. The straight line represents the linear least squares fit to these points which are represented by ○. The total flux densities estimated from our images are marked with a −.

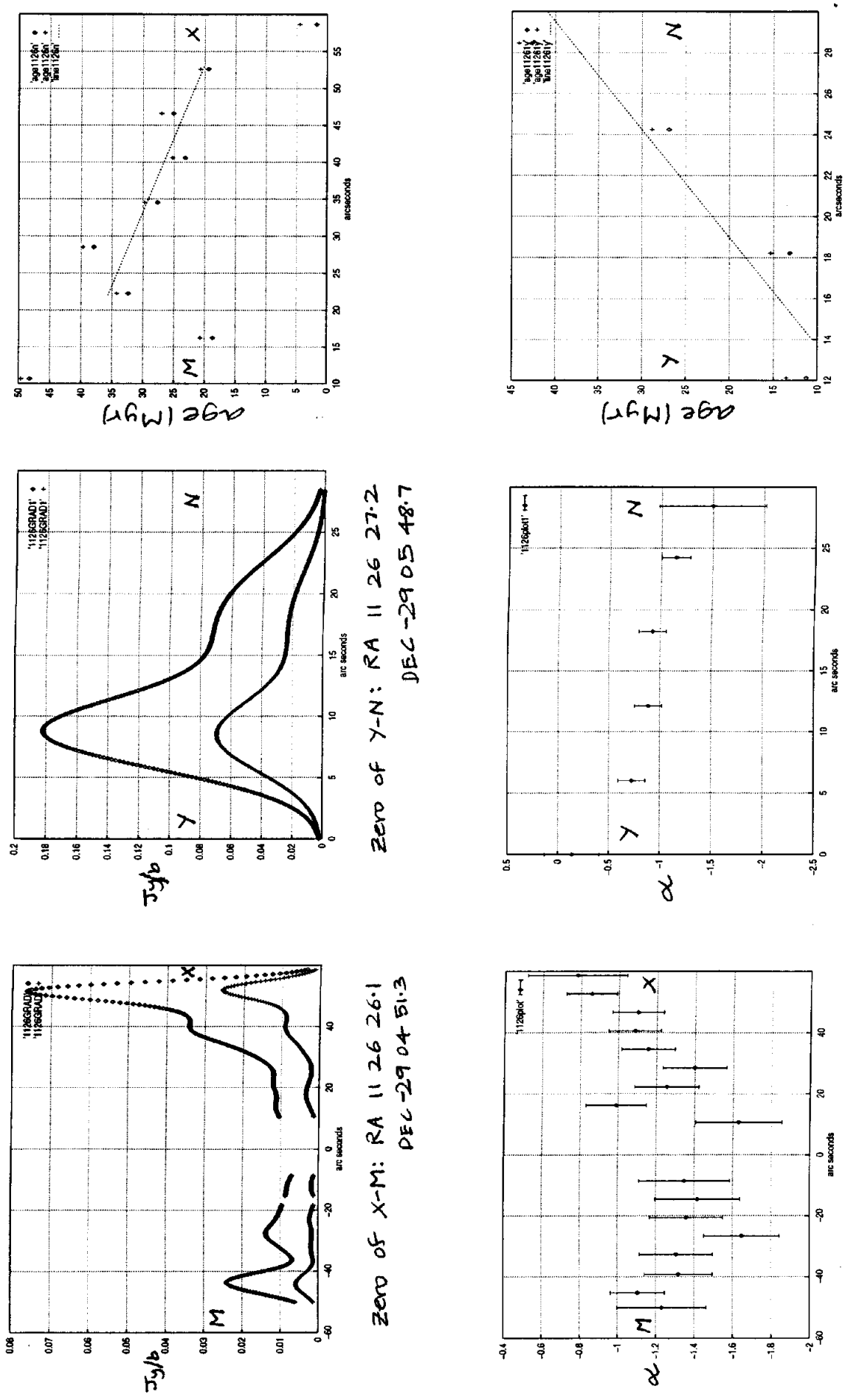

Fig. 4.3b The total intensity in L(∘) and C(+) bands, spectral-index, and age (∘ using the determined hotspot spectral-index and + using 0.75 as hotspot spectral-index) gradients along the chosen axes of 1126-290, which are marked in Fig. 4.3a.

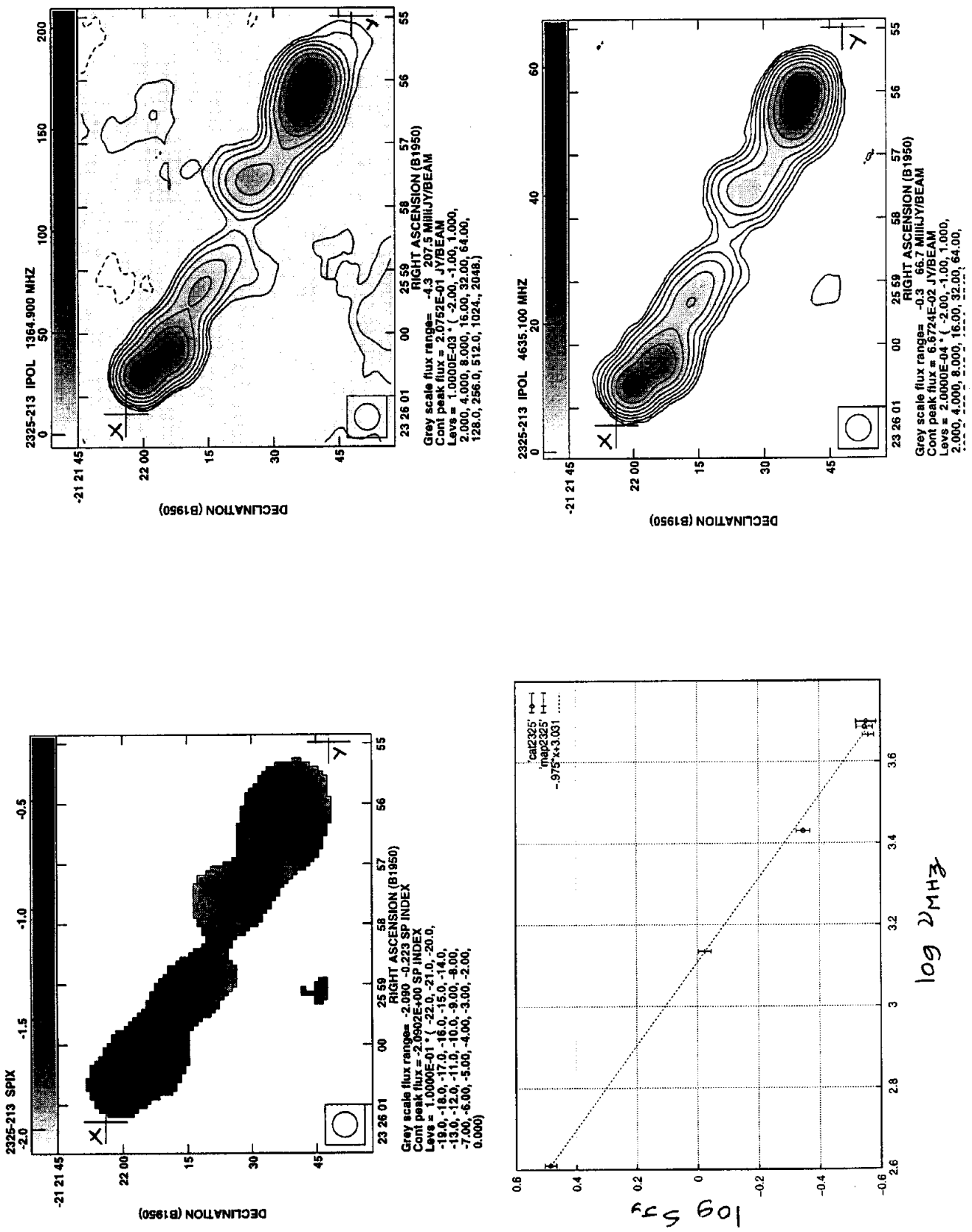

Fig. 4.4a. The L-band, C-band and spectral-index maps of 2325-213, and the radio spectrum obtained from low-resolution measurements in the literature. The straight line represents the linear least squares fit to these points which are represented by ◇. The total flux densities estimated from our images are marked with a −.

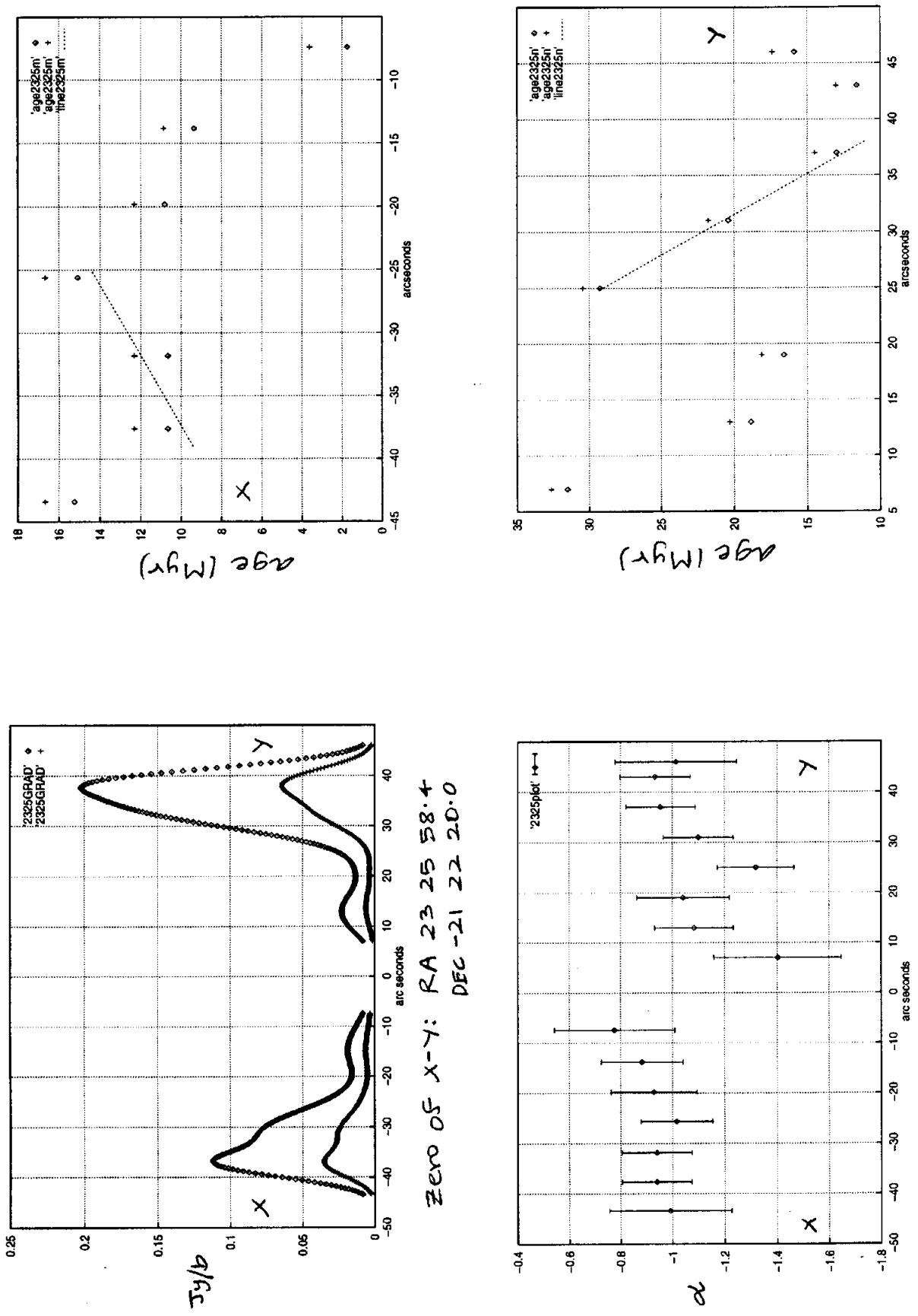

Fig. 4.4b The total intensity in L(◇) and C(+) bands, spectral-index, and age (◇ using the determined hotspot spectral-index and + using 0.75 as hotspot spectral-index) gradients along the chosen axis of 2325-213, which are marked in Fig. 4.4a.

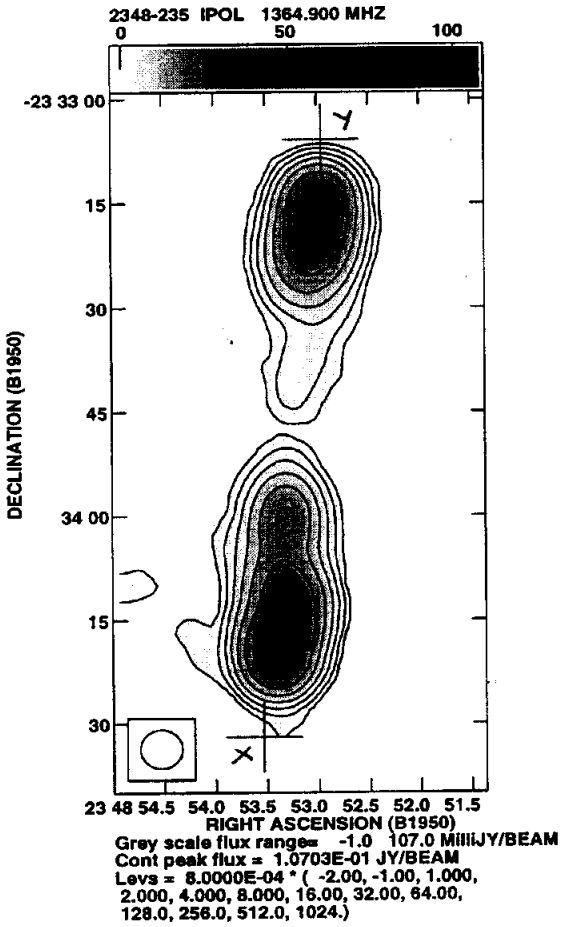

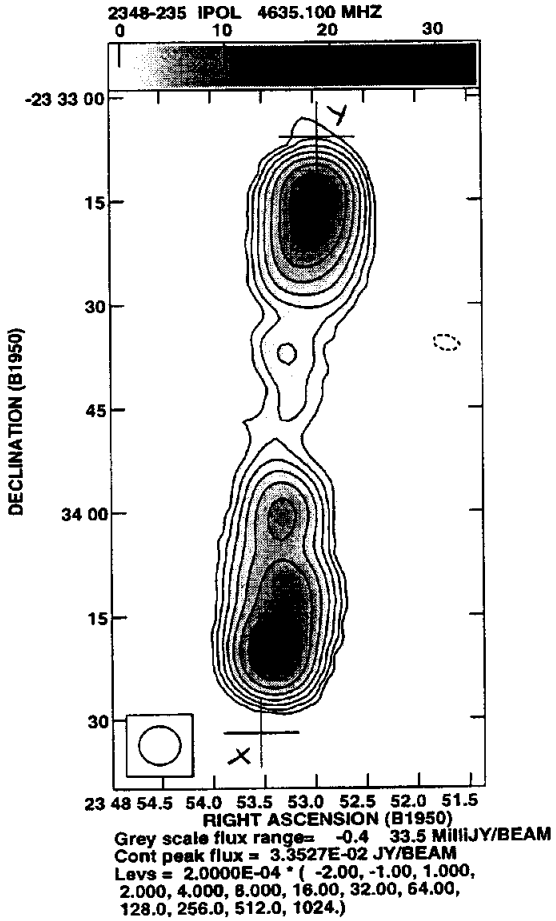

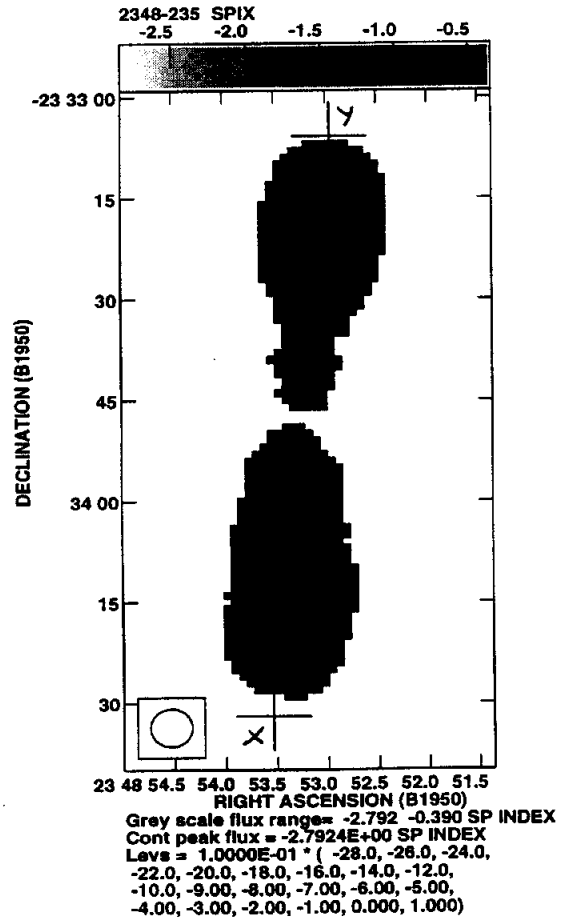

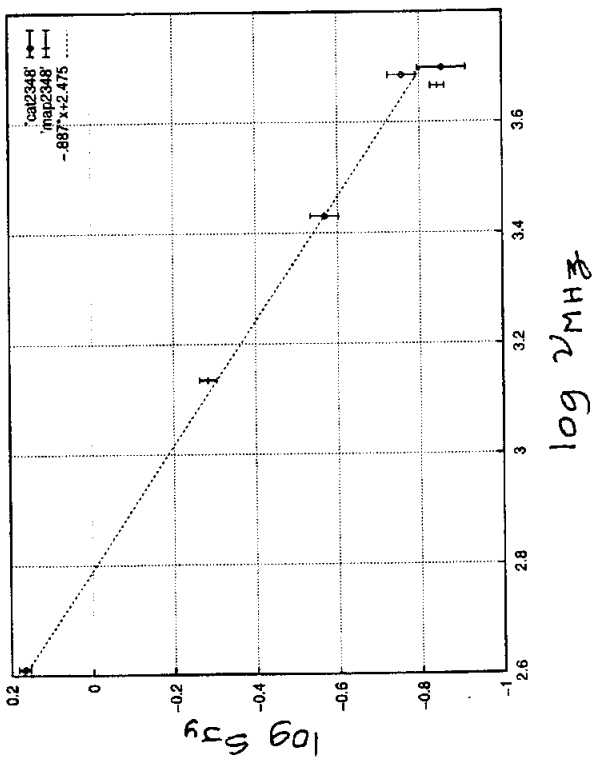

Fig. 4.5a. The L-band, C-band and spectral-index maps of 2348-235, and the radio spectrum obtained from low-resolution measurements in the literature. The straight line represents the linear least squares fit to these points which are represented by ○. The total flux densities estimated from our images are marked with a −.

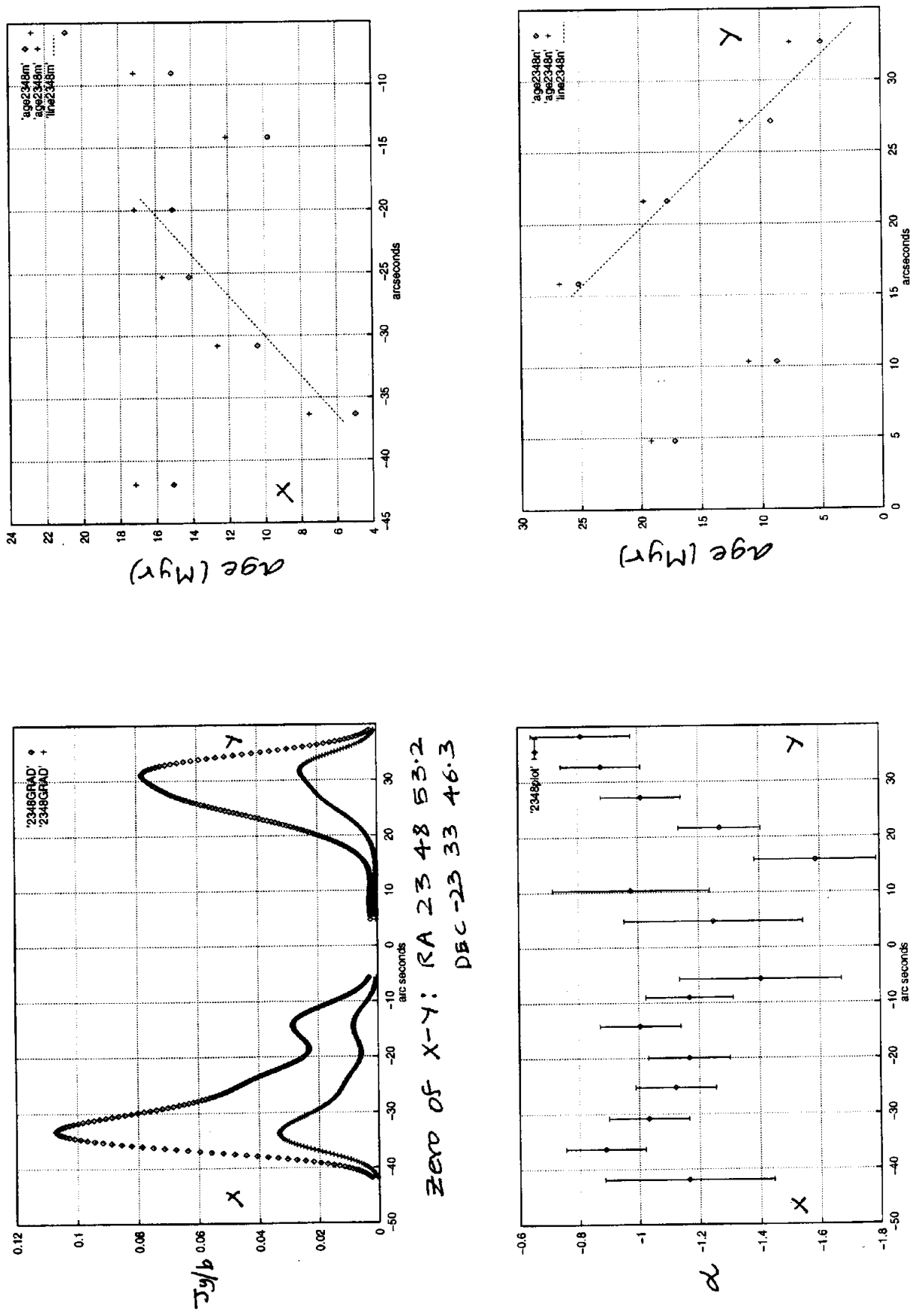

Fig. 4.5b The total intensity in L(⋄) and C(+) bands, spectral-index, and age (⋄ using the determined hotspot spectral-index and + using 0.75 as hotspot spectral-index) gradients along the chosen axis of 2348-235, which are marked in Fig. 4.5a.

Table 4.1 Flux densities and noises from the images of our sources

Source Name	rms noise$_{1365}$ mJy/b	rms noise$_{4635}$ mJy/b	$S_{t,1365}$ Jy	$S_{t,4635}$ Jy	HPBW $''$
0148-297	0.85	0.250	2.95	0.87	4.8
0428-281	0.25	0.065	0.96	0.28	5.2
1126-290	0.23	0.135	1.10	0.31	6.3
2325-213	0.82	0.067	0.94	0.28	5.8
2348-235	0.23	0.052	0.51	0.14	5.6

Table 4.2 Observational results of the sources

Source Name	Component	RA h m s	DEC ^{o} $'$ $''$	$S_{peak,1365}$ mJy/b	S_{1365} mJy	$S_{peak,4635}$ mJy/b	S_{4635} mJy
0148-297	Sp lobe	01 48 17.53	-29 47 47.0	302.9	1764.8	109.6	484.4
	Sp hotspot	01 48 17.53	-29 47 47.0	302.9	1319.7	109.6	404.0
	Nf lobe	01 48 22.67	-29 45 49.0	230.3	1284.3	85.3	363.6
	Nf hotspot	01 48 22.67	-29 45 49.0	230.3	555.5	85.3	196.4
0428-281	W lobe	04 28 14.98	-28 07 15.0	348.0	539.6	116.8	157.2
	W hotspot	04 28 14.98	-28 07 15.0	348.0	464.2	116.8	147.1
	E lobe	04 28 19.52	-28 07 05.0	259.8	430.2	80.3	116.6
	E hotspot	04 28 19.5	-28 07 05.0	259.8	366.5	80.3	108.5
1126-290	Np lobe	11 26 23.85	-29 04 09.0	76.0	325.8	25.8	82.3
	Np hotspot	11 26 23.85	-29 04 09.0	76.0	193.9	25.8	59.4
	Sf lobe	11 26 27.51	-29 05 41.0	183.7	738.4	70.6	219.2
	Sf hotspot	11 26 27.51	-29 05 41.0	183.7	417.1	70.6	145.2
2325-213	Sp lobe	23 25 56.00	-21 22 39.0	207.5	604.0	66.7	164.7
	Sp hotspot	23 25 56.00	-21 22 39.0	207.5	528.3	66.7	146.7
	Nf lobe	23 26 00.65	-21 21 60.0	125.4	344.9	39.5	109.4
	Nf hotspot	23 26 00.65	-21 21 60.0	125.4	298.8	39.5	89.1
2348-235	N lobe	23 48 52.96	-23 33 15.0	77.8	206.7	25.9	58.1
	N hotspot	23 48 52.96	-23 33 15.0	77.8	186.2	25.9	52.1
	S lobe	23 48 53.39	-23 34 19.0	107.0	302.6	33.5	84.0
	S hotspot	23 48 53.39	-23 34 19.0	107.0	289.5	33.5	81.2

4.2 Spectral ages of our sources

The brightness distributions at the two frequencies, 1365 and 4635 MHz, along the specified axes shown in the total-intensity images, the corresponding spectral indices and the estimates of the ages are presented in Figures 4.1b to 4.5b. The slices have been obtained using the task *slice* and the ages have been estimated using the formalism of Myers & Spangler (1985), which is described in Chapter 2. The relation between 2-frequency spectral index and a parameter X_0 is given as,

$$\alpha_{4.9}^{1.4} = g(X_0) \tag{25}$$

where $X_0 = (C_2^2/C_1)\nu B^3 t^2 < sin^2\theta >^2 = 2.23 \times 10^{-4}(1+z)\nu_{GHz} {B_{-5}}^3 t_{Myr}^2$, ($B_{-5}$ in units of 10^{-5} gauss). The spectral index map is used to estimate the 2-frequency spectral index $\alpha_{4.9}^{1.4}$ at different pixels. For each value of spectral index the value of the parameter X_0 is estimated from the spectral-index vs X_0 plots in Myers & Spangler (1985). For our values of the hotspot spectral indices, X_0 has been estimated by either extrapolating or interpolating between the values given by Myers & Spangler (1985). Now using the calculated value of the equipartition magnetic field, B_{eq}, the age is determined. B_{eq} has been estimated by integrating the luminosity between 10 MHz and 10 GHz, and assuming the ratio of electron to particle energy density to be unity.

The results of our estimates are presented in Table 4.3 which is arranged as follows. Column 1 lists the source while column 2 gives the the equipartition magnetic field, which has been determined assuming that it is uniform throughout the source, and that the source has a cylindrical symmetry. The spectral age calculated for X and Y lobe using the hotspot spectral index (column 3) as an initial spectral index i.e. corresponding to zero spectral age is listed in column 4. The age has also been calculated assuming that the intial spectral index is 0.75 and is listed in column 5. Hotspot spectral indices are in the range of 0.5 to 1.0 (Laing 1989), and we have made our estimates for a typical value of 0.75. The velocities estimated from the slope of a linear least squares fit to the age vs separation plot are given in column

6. Ages and velocities are calculated including the cosmic microwave background radiation, as the relativistic electrons also lose their energy through inverse Compton scattering with the background radiation. These values are listed in the next the three columns. Including the microwave background decreases the age by a factor $[1 + (B_{MWB})^2/B^2]$, where B_{MWB} is the equivalent magnetic field strength of cosmic microwave background radiation, and the velocities increase by the same factor. For each source, the first row in columns 4 to 9 (estimates of ages and velocities) refers to lobe X while the second row refers to lobe Y. The lobes X and Y are marked in Figures 4.1a to 4.5a.

Table 4.3 Derived parameters of our sources

Source Name	B_{eq} 10^{-5} G	α_0	Age 10^6 yrs	Age * 10^6 yrs	V 0.01c	Age_{MWB} 10^6 yrs	Age_{MWB} * 10^6 yrs	V_{MWB} 0.01c
0148-297	0.72	0.80	43.46	46.16	0.69	24.42	25.96	1.22
			41.16	44.24	0.33	23.12	24.86	0.58
0428-281	1.26	0.88	24.82	27.10	0.93	16.80	18.34	1.37
			25.96	28.26	0.85	17.56	19.12	1.25
1126-290	0.75	0.78	42.58	44.10	0.53	24.78	25.66	0.90
			48.10	49.50	2.00	27.98	28.80	3.44
2325-213	0.84	0.78	15.22	16.64	2.63	7.98	8.74	5.01
			31.44	32.58	0.74	16.50	17.10	1.40
2348-235	0.99	0.81	20.84	22.68	1.62	8.28	9.02	4.07
			25.12	26.72	0.81	9.98	10.62	2.03

Notes on individual sources.

0148-297: This source has the largest angular size among the 5 objects in our sample. The South preceding (Sp) lobe has double hotspots, the northern one of which is close to the axis defined by the radio galaxy and the North following (Nf) hotspot. The southern of the two hotspots is brighter and we have assumed this to be the primary hotspot from which material flows outwards to form the secondary hotspot in addition to contributing to the backflow. However, higher resolution observations and possibly the imaging of the jet would be required to establish the flow directions unambiguously. Both the southern hotspots have

similar spectral indices between $\lambda 20$ and 6cm, with the spectra steepening away from the hotspots. Similar spectra suggests that there is possibly reacceleration of particles in the secondary hotspot.

0428-281: The source is reasonably symmetric, and has a prominent bridge of emission which is seen clearly in the $\lambda 20$cm image.

1126-290: The flux density of the lobes is somewhat asymmetric with a ratio of 2.27 and 2.41 for peak brightness of the hotspots and the total emission from the lobes. There is a plume of emission in the South following (Sf) component extending towards the north-west. The southern brighter component has a double hotspot structure. We have assumed the brighter one to be the primary hotspot. The spectra steepen marginally towards the secondary hotspot.

2325-213: This galaxy has a bridge of emission almost along the entire axis of the source, which is visible at both $\lambda 20$ and 6cm. There is no significant evidence of spectral steepening in the eastern lobe, possibly because of reacceleration of particles in the lobe. The age estimate has been made from the marginal steepening close to the hotspot and should be treated with caution. The evidence of steepening close to the western hotspot is more significant.

2348-235: This is one of most symmetric sources in our sample and has an angular size of about 63 arcsec. The spectra steepen away from the hotspots but appear to flatten in the secondary peaks of emission.

4.3 Earlier estimates of spectral ages from radio images

Table 4.4 gives the list of sources from the literature for which ages and velocities have been determined from spectral-index gradients along the source. The total number of sources observed in different frequencies are given in Table 4.5. Table 4.4 lists the sources, their

frequencies of observations, linear sizes, luminosities and estimates of ages and velocities. The formulae used for calculating the luminosity at 178 MHz and the linear size are, $L(\nu)/4\pi = 0.86 \times 10^{26} S_{Jy}(z + \frac{z^2}{2})^2(1+z)^{\alpha-1} W Hz^{-1} sr^{-1}$ and $l = 14.54\theta'' \frac{z+\frac{z^2}{2}}{(1+z)^2} kpc$ for cosmological constants H_0=100 km s^{-1} Mpc^{-1} and q_0=0.

The estimates of age and velocity of our sample of 5 sources is consistent with values available in the literature for sources of similar luminosity. In Figure 4.6 we present the plot of age with total luminosity at 178 MHz. Almost all the age estimates plotted in the figure have been made using a cosmological model where the Hubble constant is 100 km s^{-1} Mpc^{-1}. There is weak evidence for the more luminous sources to be younger. For example, the median age for those with log P(178) $\geq$27.0 W Hz^{-1} sr^{-1} is about 4 Myr, while for those with lower luminosities it is about a factor of 3 larger. This could be understood in terms of an increase in B_{eq} with luminosity, so that ages will be younger for the more luminous objects.

Table 4.4 Survey of previous studies on spectral ageing

Source	Op. Id.	z	151 MHz	408 MHz	1.4 GHz	2.7 GHz	5 GHz	10.6 GHz	15 GHz	lin.size kpc	$log_{10}P_{178}$ $WHz^{-1}sr^{-1}$	age Myr	vel. .01c	remarks	ref.
0017+154 3C9	Q	2.012					y			90.5	28.45	0.17			1
0052+682 3C27			y		y		y					6.8, 9.7		b=6°, obscured	3,4
0133+207 3C47	Q	0.425			y	y	y*		y	254.4	26.77	7			5
0145+533 3C52	G	0.285			y		y			146.4	26.04		3, 3.5		3
0154+286 3C55	G	0.240	y		y					180.3	26.13	6.2, 6.8			4
0229+341 3C68.1	Q	1.238	y		y					302.4	27.57	6.2, 5.1			4
0231+313 3C68.2	G	1.575	y		y					144.0	28.16	2.2, 2.4			4
0234+590 3C69					y		y							b=-1°, obscured	3
0307+169 3C79	G	0.256			y	y	y*		y	231.3	26.33	9	6.67, 9		7,8
0404+429 3C103	G	0.330			y		y			278.2	26.49		7, 9.3		3
0501+381 3C134	G				y		y							b=-2°, obscured	3
0512+249 3C136.1	G	0.064			y	y				352.1	24.71		3, 4		3
0521+282 3C139.2					y		y							b=-4°, obscured	3
0610+261 3C154	Q	0.580			y		y			218.3	26.95	23.9, 21.3	0.7		3,4
0640+234 3C165	G	0.290			y		y			252.1	26.08		1.7, 3		3
0642+214 3C166	G	0.245			y		y			117.2	25.99		2.3, 5		3,8
0710+118 3C175	Q	0.768	y		y					237.2	27.23	17.2, 17.3			4
0833+654 3C204	Q	1.112					y			197.3	27.46	.28			1
0850+140 3C208	Q	1.110					y			62.0	27.62	.28			1
0903+169 3C215	Q	0.411					y			213.3	26.39	.83			1
0917+458 3C219	G	0.174			y	y	y*		y	377.5	26.09	20, 47	5.67, 2.3	reacc	1
0945+735 4C73.08	G	0.058	y		y	y		y		734.8	24.64	30, 900		width perpendicular	6
0958+290 3C234	G	0.185			y	y	y*		y	229.9	26.03	8	10.2, 15		5,3
1008+467 3C239	G	1.781			y		y		y	70.9	28.15		10, 13		9
1030+585 3C244.1	G	0.428			y		y			196.2	26.64		9.1, 8		3

Table 4.4 (contd.)

Source	Opt. Id.	z	151 MHz	408 MHz	1.4 GHz	2.7 GHz	5 GHz	10.6 GHz	15 GHz	lin.size kpc	luminosity $WHz^{-1}Sr^{-1}$	age MYr	vel. .01c	remarks	ref.
1040+123 3C245	Q	1.029			y		y		y	27.0	27.41		18		9
1056+432 3C247	G	.749			y		y		y	63.6	26.89		13, 10		9
1100+772 3C249.1	Q	.311	y		y					133.7	26.05	20.1, 11.4			4
1108+359 3C252	G	1.105			y		y			337.5	27.45				3
1111+408 3C254	Q	.734			y		y		y	63.5	27.22		10, 13		9
1137+660 3C263	Q	.656	y		y					204.1	26.96	10.2			4
1140+223 3C263.1	G	.824			y		y		y	22.7	26.43		26, 18		9
1142+318 3C265	G	.8108	y		y		y			393.9	27.33	12.8, 9.1	14+/-30		4,3
1143+500 3C266	G	1.275			y		y		y	25.2	27.62		16, 20		9
1147+130 3C267	G	1.144	y		y					215.9	27.58	5.6, 6.9			4
1157+732 3C268.1	G	.974	y		y					248.1	27.46	6.2, 5.1			4
1206+439 3C268.4	Q	1.4			y		y		y	65.4	27.62		24, 15		9
1218+339 3C270.1	Q	1.519			y		y		y	73.4	27.82		18, 15		9
1232+216 3C274.1	G	.422			y		y			550.8	26.56		8.5, 13		3
1241+166 3C275.1	Q	.557			y		y		y	76.8	26.89		10, 11		9
1251+159 3C277.2	G	.766			y		y			286.3	27.07		5.3, .7		3
1254+476 3C280	G	.996			y		y		y	78.9	27.6		12, 13		9
1308+277 3C284	G	.2394			y	y				443.7	25.84		5, 2.3		3
1319+428 3C285	G	.0794			y		y			138.0	24.82		2.8, 1.1		3
1336+391 3C288	G	.246			y		y		y	59.5	26.08		5, 6		9
1343+500 3C289	G	.967			y		y		y	53.9	27.27		10, 9		9
1349+647 3C292	G	.88			y		y			635.8	26.86		26, 28		4,3
1350+316 3C293	G	.452			y		y			132.8	24.36		23.5+/-40		3
1404+344 3C294	G	1.779			y		y		y	60.5	26.55		14, 18		9
1419+419 3C299	G	.367			y		y		y	38.8	26.23		21, 3		9

Table 4.4 (contd.)

Source	Opt. Id.	z	151 MHz	408 MHz	1.4 GHz	2.7 GHz	5 GHz	10.6 GHz	15 GHz	lin.size kpc	luminosity $WHz^{-1}sr^{-1}$	age Myr	vel. .01c	remarks	ref.
1420+198 3C300	G	0.270			y	y	y*		y	276.1	26.13	9	1, 2.6		5,3
1502+262 3C310	G	0.054			y	y	y			224.9	25.16		1.4, .5		3
1511+263 3C315	G	0.108			y		y			270.1	25.29		1.8, 1.5		3
1522+546 3C319	G	0.192			y		y			226.0	25.76		1.3, 3.6		3
1529+242 3C321	G	0.096								352.9	25.05				3
1533+557 3C322	G	1.681	y		y					190.2	27.44	3.7, 3,6			4
1609+660 3C330	G	0.549	y		y					262.7	27.01	9.1, 11.2			4
1618+177 3C334	Q	0.555	y		y					247.1	26.64	17.1, 14.5			4
1622+238 3C336	Q	0.927					y			115.2	27.18	1.5			1
1704+608 3C351	Q	0.371	y		y					221.0	26.32				4
1723+510 3C356	G	1.079	y		y					418.8	27.43	9.5, 10.4			4
1825+743 3C379.1	G	0.256			y		y			196.1	25.69		8.3, 5.7		8
1833+326 3C382	G	0.058			y	y	y*		y	146.0	24.77	69, 12	.6, 3.3	reacc	5
1845+797 3C390.3	G	0.056			y		y*			163.7	25.14	3.4, 7.5		prec. jets, reacc	10
1914+302 3C399.1					y		y							b=9°, obscured	3
1957+406 3C405	G	0.056	y		y		y			96.0	27.39	2.8, 3.2	1.1, .9		4,3
1958+406 cyg A			y		y		y		y			6	5		2,11
2012+234 3C409			y		y									b=-6°, obscured	4
2019+098 3C411	G	0.467			y		y			103.1	26.64		20		8
2104+763 3C427.1	G	0.572	y		y					99.9	27.08	3.8, 3.9			4
2106+494 3C428					y		y							b=1°, obscured	3
2117+606 3C430	G	0.054			y	y	y*		y	62.0	24.94	6	3, 3.1		7,8,3
2120+168 3C432	Q	1.805					y			82.4	28.04	.64			1
2243+394 3C452	G	0.081		y	y	y*	y*			262.3	25.51				5

1-Bridle et al.(1994), 2-Winter(1980), 3-Alexander & Leahy(1987),

4-Leahy et al.(1989), 5-Burch(1979), 6-Mayer(1979), 7-Burch(1977),

8-Myers & Spangler(1985), 9-Liu et al.(1992), 10-Alexander et al.(1984),

11-Carilli et al.(1991)

* - data previously published in the literature used

Table 4.5 Total number of sources observed at different frequencies

	151 MHz	408 MHz	1.4 GHz	2.7 GHz	5 GHz	10.6 GHz	15 GHz
Number of sources	20	1	78	12	66	1	22

4.4 Other velocity estimates of hotspots

The velocity of the hotspot separation is determined from its spectral age, and the linear distance between the hotspot and the region where the age has been determined, assuming that the velocity of the hotspot remains roughly constant during its lifetime. The velocity estimates range from about 0.6 to 28 times 0.01c, where c=3 $\times$ 10^8 m/s, is the velocity of light. The expansion speeds and ages of radio sources have also been constrained by the separation and brightness asymmetry of the lobes on opposite sides of the nucleus. The brightness asymmetry constrains the flow speed of the plasma while the separation ratio constrains the pattern speed, or the speed at which the structure appears to propagate outwards. Interpretations of the brightness asymmetry is often complicated by inadequate resolution of the observations, since only the hotspots are moving outwards while the lobe emission represents largely backflow from the hotspots. Also the ratio would be affected by the evolution of the individual components with age since the receding component is seen at an earlier stage of evolution. Distributions of the separation ratio yield speeds in the range of 0.1 to 0.4c for the high-luminosity Fanaroff-Riley class II sources (Longair & Riley 1979; Banhatti 1980; Macklin 1981). However, in this scenario, the approaching component should always appear farther from the nucleus, since it is seen at a later stage of evolution.

Normally it is not possible to identify the approaching component. However, if one assumes that the radio jets are relativistically beamed, then the hotspot on the jet side must be the approaching one. With this assumption Saikia (1981, 1984) examined the separation ratio of samples of radio galaxies and quasars with radio jets. There was no effect for the jet side to be longer. Hence the asymmetry must be due to other effects such as an asymmetric distribution of gas on opposite sides of the source, or selection effects due to intrinsic non-collinearity of some of the sources. McCarthy, van Breugel & Kapahi (1991) found that for galaxies there is almost always more line-emitting gas on the shorter side, suggesting that the asymmetries are largely due to an asymmetric distribution of gas. Thus, the expansion speeds are well-below the limits derived using the above analyses.

4.5 Evidence of ageing at higher frequencies

The spectral ageing due to synchrotron losses causes the break frequency to progressively move towards lower frequencies. Thus the possibility of observing the break in the frequency spectrum of the younger sources is increased if they are observed at higher frequencies. The optical synchrotron lifetimes of the hotspots of 3C285, 3C265, and 3C390.3 are found to be less than about 2000 yrs (Saslaw et al. 1978), assuming that the optical emission is due to synchrotron radiation. Spectral studies which combine radio and optical data have been done in the past. Few of the sources for which radio-optical studies have been done are 3C33, (Rudnick et al. 1981, Meisenheimer et al. 1986a); 3C273 (Meisenheimer et al. 1986b); 3C20, 3C33, 3C111, 3C123, Pictor A, 3C273, (Meisenheimer et al. 1989); Most of the hotspot spectra of these sources show a high frequency cutoff at less than 10^{14} Hz. The model fit to the low-frequency data is flat (α=0.5) which is in agreement with the prediction of first order Fermi acceleration. The typical break frequency at which the spectrum steepens by $\Delta\alpha$=0.5 is around 10^9 Hz. Infrared imaging of the sources 3C20, 3C33, 3C65, 3C111, 3C123, 3C303, and 3C405 (Meisenheimer et al. 1997) confirm the previous claim of the presence of reacceleration of particles in most hotspots.

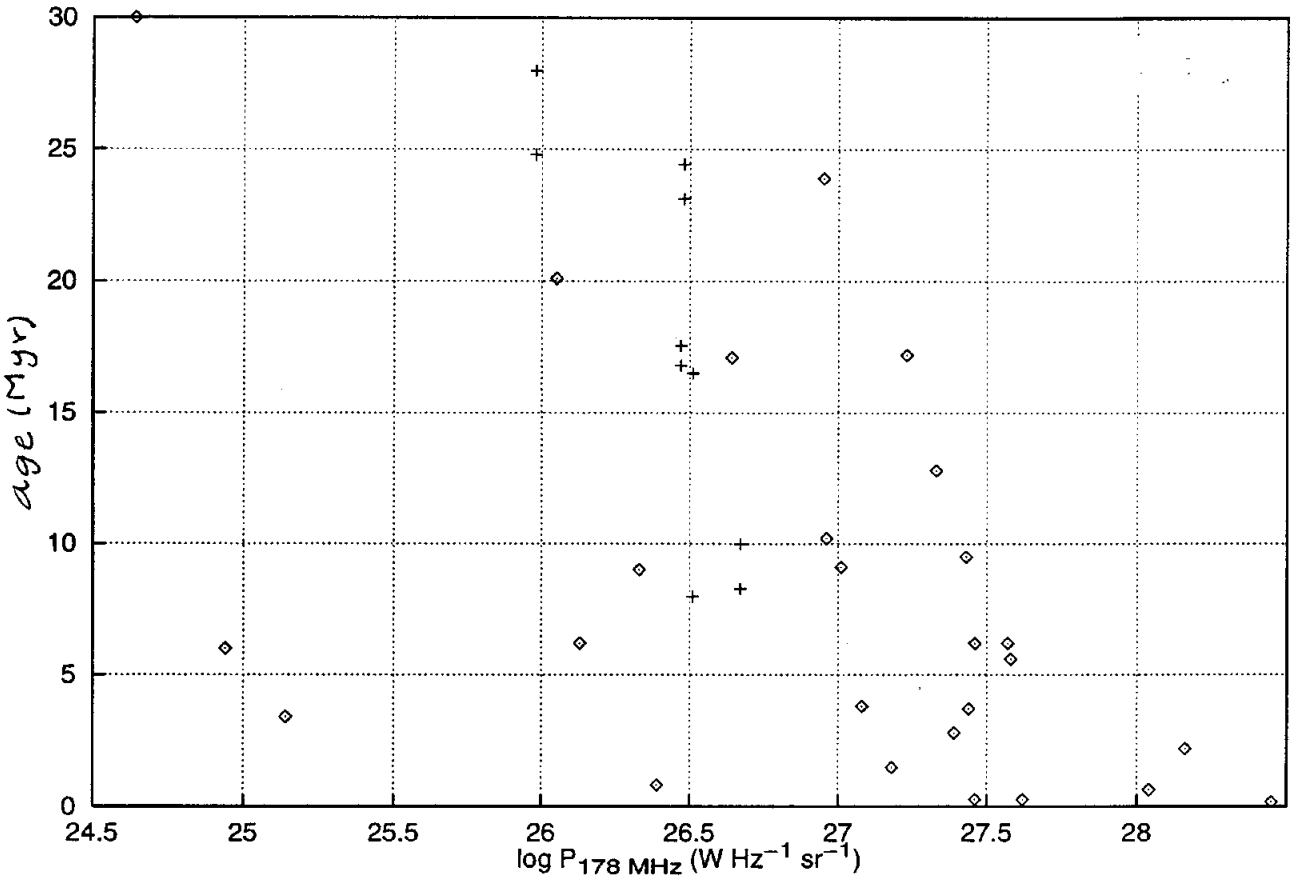

Fig. 4.6 The age-luminosity plot of our sources + along with the sources available in the literature ⋄, where the estimates have been made using cosmological model $H_0 = 100 kms^{-1} Mpc^{-1}$.

4.6 Concluding remarks

The spectral ages of the five FRII sources from the MRC catalogue are determined using the Myers & Spangler (1985) formalism which uses the 2-frequency spectral index. The sources were observed at 1365 MHz and 4635 MHz with scaled arrays using the Very Large Array. The spectral index gradients from the hotspots along the lobes are largely consistent with the standard beam model for extragalactic radio sources. The velocity and age estimates of our sources are consistent with earlier estimates of FRII sources with a similar luminosity. The source ages are around 8-28 Myr and velocity of the lobes are around 0.5-5 in units of 0.01c (c= 3×10^{8} m/s), including both synchrotron and inverse-Compton losses due to the microwave background radiation.

References

Alexander, P., Brown, M.T. & Scott, P.F., 1984, MNRAS, **209**, 851.

Alexander, P., 1987, MNRAS, **225**, 27.

Alexander, P. & Leahy, J.P., 1987, MNRAS, **225**, 1.

Baum, S.A., Zirbel, E.L. & O'Dea, C.P., 1995, Astrophys. J., **451**, 88.

Banhatti, D.G., 1980, AA, **84**, 112.

Blandford, R.D. & Rees, M.J., 1974, MNRAS, **169**, 395.

Bridle, A.H., Hough, D.H., Lonsdale, C.J., Burns, J.O. & Liang, R.A., 1994, Astronomical J., **108**,766.

Burch, S.F., 1977, MNRAS, **180**, 623.

Burch, S.F., 1979, MNRAS, **186**, 519.

Carilli, C.L., Perley, R.A., Dreher, J.W. & Leahy, J.P., 1991, Astrophys. J., **383**, 554.

Charles, P.A. & Seward, F.D., 1995, Exploring the X-ray Universe, Cambridge University Press.

Clements, D.L. & Pérez-Fournon, I., 1997, eds. ESO Astrophysics Symposia: Quasar Hosts, Springer.

Condon, J.J., 1988, Galactic and Extragalactic Radio Astronomy, eds Verschuur, G.L. & Kellerman, K.I., Springer-Verlag.

Fanaroff, B.L. & Riley, J.M., 1974, MNRAS, **167**, 31p.

Heavens, A.F. & Meisenheimer, K., 1987, MNRAS, 225, 335.

Kardashev, N.S., 1962, Soviet Astronomy-AJ, **6**, 317.

Kellermann, K.I., 1966, Astrophys. J., **146**, 621.

Jaffe, W.J. & Perola, G.C., 1973, Astr. Astrophys., **26**, 423.

Large, M.I., Mills, B.Y., Little, A.G., Crawford, D.F. & Sutton, J.M., 1981, MNRAS, **194**, 693.

Laing, R.A. 1989, in Hot Spots in Extragalactic Radio Sources, eds Meisenheimer, K. & Röser, H.-J., Springer-Verlag, p. 27.

Leahy, J.P., Muxlow, T.W.B. & Stephens, P.W, 1989, MNRAS, **239**, 401.

Liu, R., Pooley, G. & Riley, J.M., 1992, MNRAS, **257**, 545.

Longair, M.S., & Riley, J.M., 1979, MNRAS, **188**, 625.

Longair, M.S., 1994, High Energy Astrophysics Vol.1 and 2, Cambridge University Press.

Macklin, J.T., 1981, MNRAS, **196**, 967.

Mangalam, A.V. & Gopal-Krishna, 1995, MNRAS, **275**, 976.

Mayer, C.J., 1979, MNRAS, **186**, 99.

McCarthy, P.J., van Breugel, W. & Kapahi,V.K., 1991, Astrophys. J., **371**, 478 .

McCarthy, P.J., Kapahi, V.K., van Breugel, W., et al., 1996, Astrophys. J. (Supp.), **107**, 19.

Meisenheimer, K. & Roser, H.-J., 1986a, Nature, **319**, 459.

Meisenheimer, K. & Heavens, A.F., 1986b, Nature, **323**, 419.

Meisenheimer, K., Roser, H.-J., Hiltner, P.R., et al., 1989, Astr. Astrophys., **219**, 63.

Meisenheimer, K., Yates, M.G. & Roser, H.J., 1997, Astr. Astrophys., **325**, 57.

Myers, S.T. & Spangler, S.R., 1985, Astrophys. J., **291**, 52

Pacholczk, A. G., 1970, Radio Astrophysics, W. H. Freeman and Company.

Padmanabhan, T., 1993, Structure formation in the universe, Cambridge University Press.

Perley, R.A., Willis, A.G. & Scott, J.S., 1979, Nature **281**, 437.

Perley, R. A., and Taylor, G. B., 1996, The VLA Calibrator Manual, NRAO.

Rudnick, L., Saslaw, W.C., Crane, P. & Tyson, J.A., 1981, Astrophys. J., **246**, 647.

Sahni, V. & Coles, P., 1995, Physics Reports, **262**, 1.

Saikia, D.J., 1981, MNRAS, **197**, 11P.

Saikia, D.J., 1984, MNRAS, **209**, 525.

Seyfert, C., 1943, Astrophys. J., **97**, 28.

Saslaw, W.C., Tyson, J.A. & Crane, P., 1978, Astrophys. J., **222**, 435.

Scheuer, P.A.G., 1995, MNRAS, **277**, 331.

Scheuer, P.A.G. & Williams, P.J.S., 1968, ARAA, **6**, 321.

Tribble, P.C., 1993, MNRAS, **261**, 57.

Winter A.J.B., Wilson, D.M.A., Warner, P.J., et al., 1980, MNRAS, **192**, 931.

Wiita, P.J. & Gopal-Krishna, 1990, Astrophys. J., **353**, 476.

Wright, A.E. & Otrupcek, R.E., PKSCAT90, Version V 1.01.

Zensus, J.A. & Pearson, T.J., 1990, Parsec-scale radio jets, Cambridge University Press.

Zensus, J.A., Krichbaum, T.P., Lobanov, A.P., 1995, Proc. Natl. Acad. Sci., **92**, 11348

Zirbel, E. & Baum, S.A., 1995, Astrophys. J., **448**, 521.